Master's thesis

Czech
Technical
University
in Prague

F3

Faculty of Electrical Engineering
Department of Computer Science

3D reconstruction from Compton camera images

Vojtěch Poříz

Supervisor: prof. Dr. Ing. Jan Kybic
May 2023

MASTER‘S THESIS ASSIGNMENT

I. Personal and study details

Student's name:	**Poříz Vojtěch**	Personal ID number:	**474385**
Faculty / Institute:	**Faculty of Electrical Engineering**		
Department / Institute:	**Department of Computer Science**		
Study program:	**Open Informatics**		
Specialisation:	**Artificial Intelligence**		

II. Master’s thesis details

Master’s thesis title in English:

3D image reconstruction from Compton camera

Master’s thesis title in Czech:

Rekonstrukce 3D obrazu z Comptonovy kamery

Guidelines:

The task is to develop a method for 3D image reconstruction of the thyroid gland radionuclide examination from Compton camera images.
Familiarize yourself with Compton camera.
Review existing simulators and test them. If needed, create your own simulator. Create a suitable dataset using both simulated and real data.
Review existing Compton camera reconstruction methods and select one or two most promising ones.
Implement the chosen method(s) of reconstruction and verify its performance experimentally. Optimize and accelerate the code.
Propose, implement and test improvements of the reconstruction method using regularization or a learning-based method.
Evaluate the performance of the improved method.

Bibliography / sources:

Tashima H, Yamaya T. Compton imaging for medical applications. Radiol Phys Technol. 2022 Sep;15(3):187-205
Kenneth Lange and Richard Carson, “EM reconstruction algorithms for emission and transmission tomography”. J. Comput. Assist. Tomogr, 8(2):306–316, 1984.
Feng, Yuemeng, “Modeling and regularization in tomographic reconstruction for Compton camera imaging”, PhD. Thesis, INSA Lyon, 2019.
A. J. Reader, G. Corda, A. Mehranian, C. d. Costa-Luis, S. Ellis and J. A. Schnabel, "Deep Learning for PET Image Reconstruction," in IEEE Transactions on Radiation and Plasma Medical Sciences, vol. 5, no. 1, pp. 1-25, Jan. 2021, doi: 10.1109/TRPMS.2020.3014786.

Name and workplace of master’s thesis supervisor:

prof. Dr. Ing. Jan Kybic Biomedical imaging algorithms FEE

Name and workplace of second master’s thesis supervisor or consultant:

Date of master’s thesis assignment: **31.01.2023** Deadline for master's thesis submission: **26.05.2023**

Assignment valid until: **22.09.2024**

prof. Dr. Ing. Jan Kybic
Supervisor’s signature

Head of department’s signature

prof. Mgr. Petr Páta, Ph.D.
Dean’s signature

III. Assignment receipt

The student acknowledges that the master’s thesis is an individual work. The student must produce his thesis without the assistance of others, with the exception of provided consultations. Within the master’s thesis, the author must state the names of consultants and include a list of references.

.
Date of assignment receipt

Student’s signature

Acknowledgements

First and foremost, I would like to express sincere appreciation to my supervisor, prof. Jan Kybic, for his kind guidance, invaluable insights and undying willingness to help.

Furthermore, I would like to express my gratitude to the CTU FEE for providing me with an excellent wealth of knowledge to start my career.

I would also like to extend my heartfelt thanks to the members of the ThyroPIX team, who introduced me to the field of Compton cameras and provided crucial help with the organization of the real experiments.

I am profoundly grateful to my loving family, Marie, Martin and Vítek, for their endless belief in my abilities and encouragement throughout my childhood and academic journey. Their sacrifices to ensure my success were instrumental, and I hope I will be able to give them back.

A big thank you belongs also to my friends and schoolmates, for their unwavering laughter and support, which made these intense years of study somewhat enjoyable. I am grateful for the memories we have created together and look forward to many more.

Last but certainly not least, I would like to express my deepest appreciation to Pája, for being my shoulder to lean on and always bringing the much needed smile and encouragement to keep going.

Declaration

I hereby declare that the presented work was developed independently and that I have listed all sources of information used within it in accordance with the Methodical instructions for observing the ethical principles in the preparation of university thesis.

Prague, May 26, 2023

Abstract

Thyroid cancer is a prevalent disease, and nuclear imaging methods play a vital role in its diagnosis and treatment. However, the current imaging modalities, such as SPECT and PET, have limitations in terms of size, cost, sensitivity and tracer flexibility, hindering their widespread usage and impeding progress in clinical understanding of the treatment. In this context, the Compton camera, with its smaller size, reduced cost, higher sensitivity and capability to handle multiple tracers emerges as a potential alternative for diagnosing various cancer types.

This thesis addresses the development of a 3D image reconstruction method for radiopharmaceutical distribution from Compton data. The proposed solution aims to meet the practicality criteria of medical radionuclide examination.

A Monte Carlo simulator is developed to generate synthetic data, and a baseline reconstruction method is established. Through computational optimization and regularization techniques, the reconstruction method is refined. Evaluation is conducted on both synthetic and real data.

The proposed method exhibits comparable qualitative performance to state-of-the-art methods, while being versatile and time-sensitive. The experimental evaluation demonstrates its practical usefulness and potential for incorporation into a clinical solution.

Keywords: Compton camera, thyroid cancer, list-mode data, MLEM, MAPEM, total variation

Supervisor: prof. Dr. Ing. Jan Kybic
Biomedical imaging algorithms, FEE

Abstrakt

Rakovina štítné žlázy je rozšířené onemocnění a nukleární zobrazovací metody hrají významnou roli v jejím diagnostikování a léčbě. Použití klasických zobrazovací modalit SPECT a PET je omezené velikostí, náklady, využitelností tracerů a citlivostí, což brání jejich širokému využití a zpomaluje pokrok v porozumění průběhu léčby. V této souvislosti se jako potenciální alternativa pro diagnostiku různých typů rakoviny objevuje Comptonova kamera, která má menší velikost, snížené náklady, vyšší citlivostí a umožňuje pracovat s více tracery.

Tato práce se zabývá vývojem 3D rekonstrukční metody obrazu pro zobrazení radioléčiv z dat získaných Comptonovou kamerou. Navrhované řešení si klade za cíl splnit praktická kritéria pro medicínské použití.

Byl vyvinut Monte Carlo simulátor pro generování syntetických dat a vytvořena základní rekonstrukční metoda. Prostřednictvím výpočetní optimalizace a regularizačních technik byla rekonstrukční metoda vylepšena. Evaluace byla provedena jak na syntetických, tak na reálných datech.

Navrhovaná metoda vykazuje srovnatelné kvalitativní výsledky s nejlepšími dostupnými metodami, přičemž je zároveň všestranná a respektuje časová omezení. Experimentální hodnocení ukazuje její praktickou užitečnost a potenciál pro začlenění do klinického řešení.

Klíčová slova: Comptonova kamera, rakovina štítné žlázy, list-mode data, MLEM, MAPEM, total variation

Překlad názvu: Rekonstrukce 3D obrazu z Comptonovy kamery

Contents

Chapter 1

Introduction

1.1 Motivation

Thyroid cancer is among the most prevalent cancers in young adults. The diagnostics is usually accommodated by nuclear imaging methods. If diagnosed early, a simple surgical extraction of the thyroid can be completely curative. In the later stages of thyroid cancer, where nodules are formed, radionuclide therapy is needed to remove these residues.

Currently used nuclear imaging modalities include SPECT and PET. These systems are large in size, expensive, do not provide sufficient spatial resolution to detect some of these residues, are limited to only one tracer at a time, and do not allow measurements at high photon fluxes at a high activity rate. Because of this, they cannot be employed regularly in cancer patients, hindering their treatment options as well as research progress in the clinical understanding of the treatment dynamics.

An alternative detector called the Compton camera shows promising potential by providing high sensitivity, a wide field of view, and the ability to work with multiple traces at once. Moreover, due to its small size and reduced cost, it could be utilized for diagnostics of patients suffering from a wide spectrum of cancer types.

A research project called ThyroPIX was proposed by a consortium of academic, clinical and industrial institutions to explore the potential of Compton cameras for thyroid cancer patients. The main goal was to build a prototype of a healthcare device for detecting thyroid remnants and nodes.

1.2 Problem statement

The task of this thesis is to develop a 3D image reconstruction method of the radiopharmaceutical distribution from Compton camera images. The main application is the imaging of ^{131}I distribution in thyroid remnants and nodules in thyroid cancer using the Compton camera developed in the ThyroPIX project. The nature of this task implies several criteria for the solution. Namely, the reconstruction must run in a reasonable time (the existing examination method takes around 20 minutes), work with the amount and quality of Compton data obtained during a typical examination of the thyroid ($10^5 - 10^6$ Compton events) and be compatible with the ThyroPIX Compton camera system.

1.3 Thesis structure

The thesis is structured as follows:

Chapter 2 provides a background information on the medical and physical aspects and introduces the imaging modalities.

Chapter 3 introduces notation and datasets. Furthermore, it contains information about the existing simulators and a description of the proposed simulator.

In Chapter 4, the theoretical foundations of the proposed reconstruction methods are laid. In adition to that, the chapter discusses the related work and state of art.

In Chapter 5, the author presents the proposed reconstruction methods with their description.

Chapter 6 contains the results of the individual methods as well as of the complete solution, demonstrated on experiments.

Chapter 7 then highlights the important findings, presents a comparison with existing approaches and concludes this thesis with a summary and a proposal for future work.

Appendix A contains the details of the implementation and project structure.

Appendix B contains the details of an experimental integration of a learning-based method.

Chapter 2

Background

2.1 Medical background

Anatomy

The thyroid gland, an essential component of the endocrine system responsible for hormone production, is situated in the neck, beside the trachea, below the larynx. The thyroid has an overall characteristic shape, resembling a butterfly, which is easily recognizable in various imaging modalities - see Figure 2.1. In adults, each thyroid lobe usually measures around 4-5 cm in height, 2 cm in width, and 2 cm in thickness, weighing approximately 20-30 g. However, pathologies affecting the gland can cause significant enlargement, sometimes weighing up to 500 g [1].

Physiology

The thyroid gland synthesizes and secretes thyroid hormones, which are integral to numerous physiological processes including normal brain development, childhood growth, female reproductive system, bone development, and mitochondrial activity [3].

Pathology

Well-differentiated papillary thyroid cancer is the most prevalent endocrine malignancy, accounting for 96.0% of all endocrine cancers and 66.8% of endocrine cancer-related deaths [4]. Most thyroid cancer forms are not aggressive and have an excellent prognosis [3]. Thyroid pathologies are visualized in Figure 2.2.

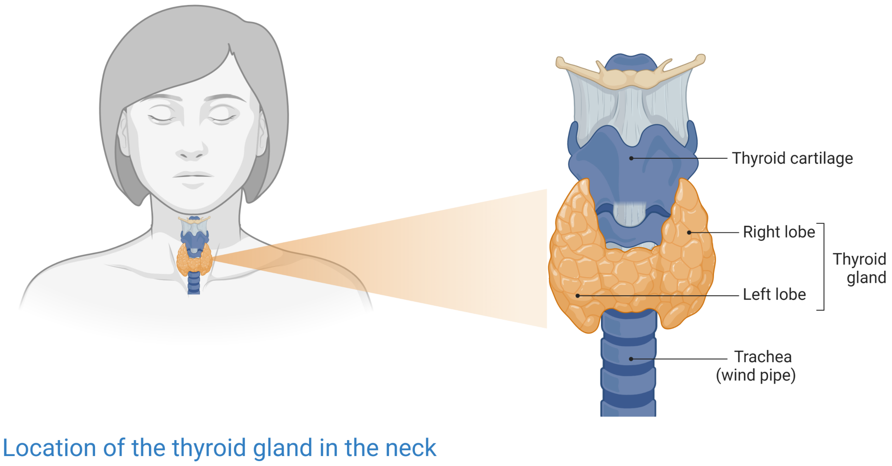
Location of the thyroid gland in the neck

Figure 2.1: Thyroid anatomy, source [2].

Symptoms

Dysfunction of the thyroid gland can manifest in various signs and symptoms across multiple organ systems [3]. Thyroid nodules, often detected during physical examinations, are the first signs of most thyroid cancers [4].

Diagnostics

The first-line test for assessing thyroid function is a blood test, followed by ultrasonography as a second diagnostic step. In case of a suspected finding, nuclear medicine is regarded as the gold standard in thyroid pathology diagnostics. Nuclear medicine imaging utilizes small amounts of radioactive stances, referred to as radiopharmaceuticals, which are injected, inhaled, or ingested by the patient. By monitoring the distribution and uptake of these radiopharmaceuticals in the body, nuclear medicine imaging can offer valuable information about the function of the thyroid. Pathological thyroid nodules can be either cold - producing too little thyroid hormone - or hot - producing too much thyroid hormone [3].

Treatment of thyroid cancer

Thyroid cancer is usually treated through surgery as a first resort. Surgical procedures aim to remove the whole thyroid gland or its parts. Following surgery, ^{131}I may be used as a treatment option, with the aim to destroy any

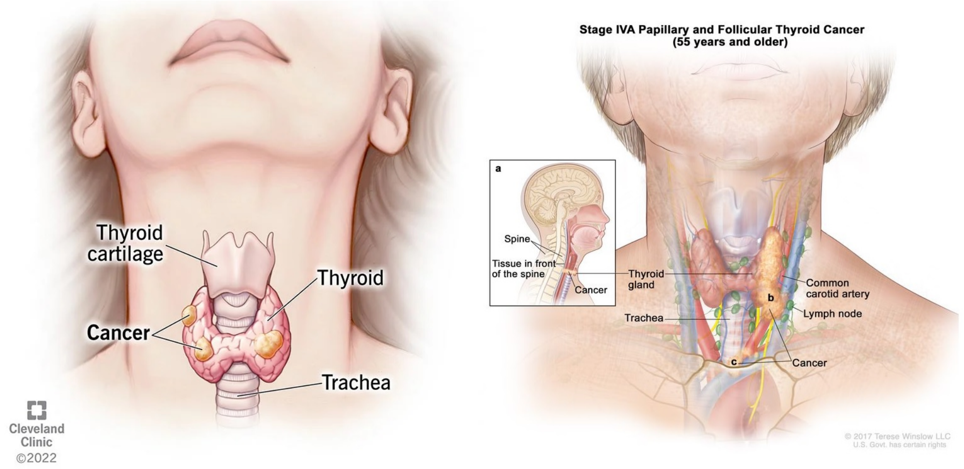

Figure 2.2: Thyroid cancer, sources [5], [6].

residual thyroid tissue and prevent recurrence [7]. The most common method for ^{131}I therapy is the administration of a large and fixed-dose, regardless of the percentage uptake of ^{131}I or treatment response of the patient [8].

2.2 Physical background

In the realm of nuclear medicine, the atom is considered the primary constituent of matter, consisting of a dense nucleus that contains neutrons and protons, surrounded by a sparse cloud of electrons. The atomic number (Z) corresponds to the number of protons in the nucleus. The atomic mass number, also called nucleon number (A), corresponds to the number of protons and neutrons in the nucleus. Isotopes are atoms sharing the same atomic number yet differing in the number of neutrons. A nuclide refers to a collection of atoms with the same number of neutrons and protons. Stability among different nuclides varies, with some inherently stable and others unstable radionuclides. Unstable radionuclides achieve stability through radioactive decay, a process that leads to a stable configuration. The decay type largely depends on the presence of either a neutron excess or deficiency compared to a stable configuration.

Radioactive decay

There are three main types of decay.

- One type of decay is alpha decay, which involves the emission of an alpha particle consisting of two protons and two neutrons from the nucleus of an atom. Radon (^{222}Rn) is a well-known example of a radioisotope that undergoes alpha decay. Alpha particles, being heavy, can only travel a short distance of a few centimetres in the air and are incapable of penetrating the skin or clothing, posing a low health risk if they remain outside the body.

- Beta decay represents another decay type. Beta particles are ionizing radiation comprising high-energy, electrically charged subatomic particles - fast-moving positrons or electrons (β^+ or β^-). β^- decay occurs when a neutron changes into a proton, emitting an electron and an antineutrino. An example of β^- decay is the first step of iodine (^{131}I) decay. On the other hand, β^+ decay occurs when a proton changes into a neutron, emitting a positron and a neutrino. While beta particles can travel several meters through the air, they can be stopped by a thin sheet of aluminium or a few centimetres of wood.
- The third type of decay is gamma decay. Gamma decay results in the emission of photons, which are typically shorter in wavelength than X-rays. A nucleus in an excited state emits excess energy in the form of one or more gamma rays. Although gamma radiation is a form of ionizing radiation, it is less ionizing compared to alpha or beta radiation [3].

The types of decay are summarized in Figure 2.3. The energy of gamma rays is measured in kiloelectron volts (keV). One electron volt is the energy required to move one electron through an electric potential difference of one Volt. Gamma rays are considered to be radiation with photon energies above 10 keV [9]. The rate at which nuclear decays occur is called radioactivity. The SI unit for radioactivity is the becquerel (Bq), which equates to 1 transformation per second.

Interaction of radiation with matter

Radiation interactions with matter are vital in nuclear medicine, with three important effects being the photoelectric effect, Compton scattering and pair production. They occur when a flying incident photon hits an atom. Each interaction's probability differs based on the incident photon's energy and the material's atomic number - see Figure 2.4. A simple scheme is presented in Figure 2.5.

The photoelectric effect occurs when a photon (with energy between a few keV and approximately 1 MeV [11]) interacts with one of the orbital electrons of an atom, causing the atom to absorb the entire energy of the incident photon. This energy exceeds the electron's binding energy, leading to the electron's release and disappearance of the initial photon. A free electron then substitutes the ejected electron. This interaction is more probable when a low-energy photon strikes a substance with a high atomic number.

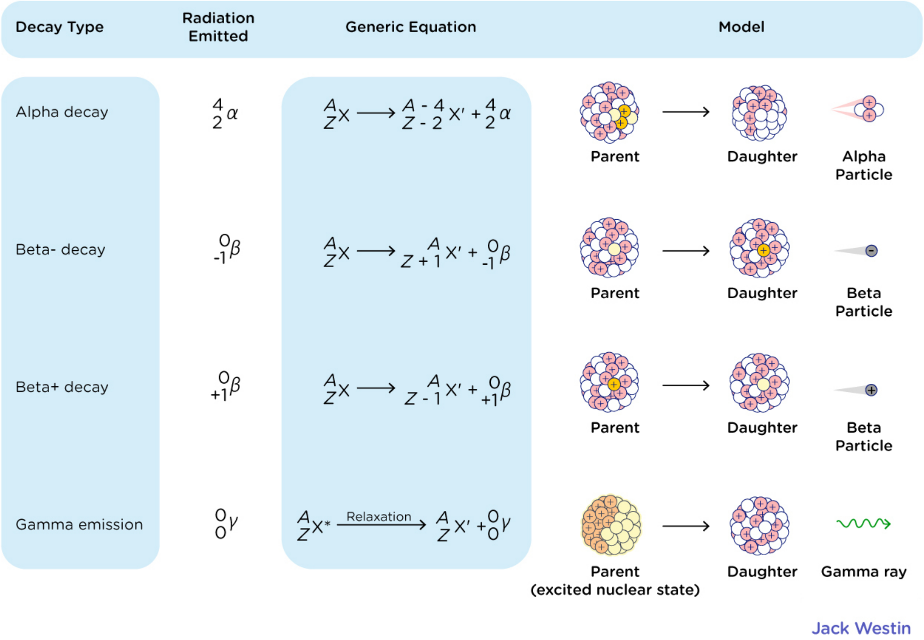

Figure 2.3: Types of radioactive decay, source [10].

Compton scattering (incoherent scattering) is an inelastic interaction between the incident photon and an electron. An electron partially absorbs the incident photon's energy, resulting in a photon with lower energy than the initial photon. Furthermore, the collision causes the photon and electron to deviate at an angle dependent on the incident photon's energy. This interaction is probable in elements with low atomic numbers and high photon energy (several tens of keV to MeV) [12].

Pair production occurs when the incident photon has high energy (more than 1.022 MeV [11]). The photon is entirely absorbed, and its energy is converted into creating an electron-positron pair and the kinetic energy of the newly created pair. After the creation, the electron annihilates with the positron, releasing two gamma rays (with energy of 511 keV) in mutually opposite directions. [13]

Radiopharmaceuticals

The most commonly employed radionuclide in the thyroid gland for diagnostic and therapeutic purposes is iodine (^{131}I) [4]. Upon decay, it emits beta particles and gamma rays. Gamma rays have different energies, 82% with an energy of 364 keV. ^{131}I has a physical half-life of 8.04 days.

Another important thyroid radionuclide is technetium (^{99}Tc). It emits gamma rays, 89% with an energy of 141 keV and has a physical half-life of 6

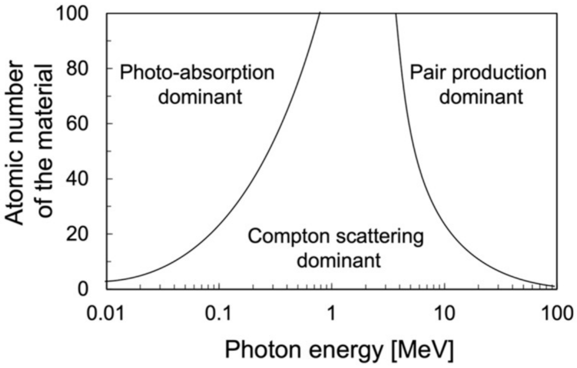

Figure 2.4: Dominant interactions with matter, source [12].

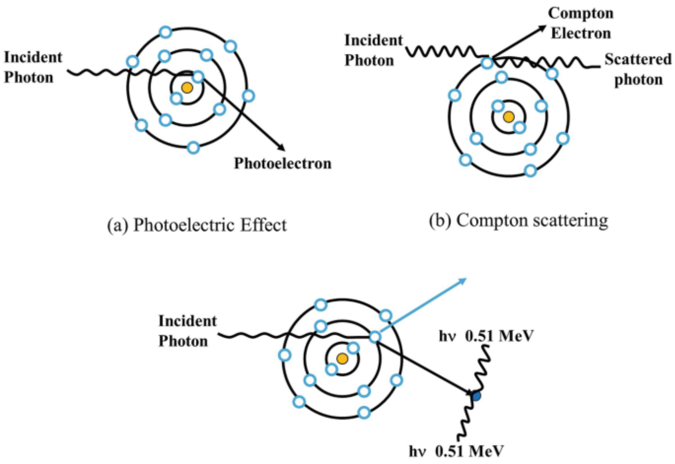

(a) Photoelectric Effect

(b) Compton scattering

(c) Pair Production

Figure 2.5: Types of radioactive decay, source [14].

h.

^{131}I and ^{99}Tc are used with gamma cameras and SPECT imaging. In case of PET imaging, a positron-emitting radioisotope fluorine (^{18}F) is broadly used [3].

2.3 Imaging modalities

The primary function of nuclear medicine imaging methods is to display a 2D/3D image of the distribution of the concentration of the radiopharmaceuticals in the body. There are two possible classical modalities - Single-photon emission computed tomography (SPECT) and Positron Emission Tomography (PET).

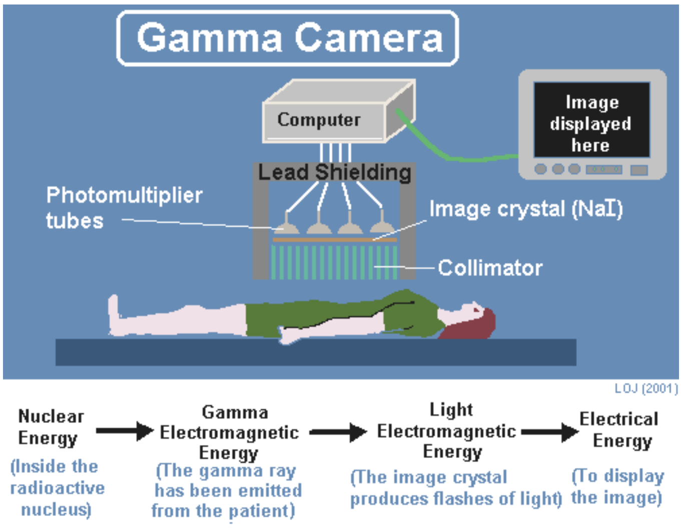

Figure 2.6: Principle of a gamma camera, source [15].

2.3.1 Gamma camera

A gamma camera is an elementary device for imaging gamma sources. See Figure 2.6 for a visualization. Gamma camera consists of a detector, a scintillator and a collimator. Positioned nearest to the patient is the collimator, which permits photons from a perpendicular direction to pass through to the crystal. Here, the photon undergoes scintillation, and the measured values are converted into electrical signals for processing. The use of collimators is essential for image reconstruction. However, it also reduces the detector's sensitivity [3]. Various collimator types exist depending on photon energy, and there is always a design trade-off between sensitivity and resolution [12][13].

2.3.2 SPECT

Single-Photon Emission Computed Tomography (SPECT) represents a tomographic imaging system. As a scintigraphic method, SPECT tracks gamma rays emitted by radiopharmaceuticals. The radioactive material is administered to the patient and emits gamma photons captured by a gamma camera detector.

SPECT acquires planar images from multiple angles, either with multiple gamma cameras or with a rotating gamma camera. During imaging, each projection takes 15-20 seconds, and there are about 30-120 projections [16]. The average examination time is 15-20 minutes [17]. The captured images are reconstructed to produce either a 2D tomographic image or a 3D image of the radiopharmaceutical distribution in the tissue. The resolution is in the order of 10-20mm [16] [18].

Modern SPECT systems frequently integrate low-dose CT scanners to enable the display of both anatomical and functional properties [3].

2.3.3 PET

Positron Emission Tomography (PET) is an alternative nuclear imaging system. PET utilizes a β^+ emitter, usually ^{18}F, that generates positrons. During the decay, generated positrons annihilate with nearby electrons, producing two gamma radiation photons that travel in opposite directions with the same energy. This property is then utilized in the detection process. A PET scanner is composed of a ring of detectors that captures photons. The PET scanner identifies corresponding photon pairs using their time of arrival. When the system detects these two photons, it generates a so-called line of response - a path between two detectors used to localize the tracer. PET then superimposes numerous lines of response from different angles for reconstruction. Similar to SPECT, modern PET systems employ additional CT for better reconstruction outcomes [9]. Compared to SPECT, PET has higher sensitivity and spatial resolution (around 10 mm [16]), corresponding to clearer pictures obtained in shorter acquisition times [13]. On the other hand, PET is more costly to operate. Figure 2.7 shows the physical differences between PET/SPECT, Figure 2.8 shows typical images obtained.

© MAYO FOUNDATION FOR MEDICAL EDUCATION AND RESEARCH. ALL RIGHTS RESERVED.

Figure 2.7: Photo of a SPECT (left) and PET (right) system, sources [19], [20].

2.3.4 Compton camera

A Compton camera is a gamma ray detection device that utilizes Compton scattering to determine the distribution of gamma ray sources. The device consists of two separate sub-detectors: the scatterer, which primarily facilitates Compton scattering and is generally made of low atomic number material, and the absorber, which predominantly facilitates the photoelectric effect and is typically constructed from high atomic number material. By analyzing the series of interactions between incoming gamma ray photons and the sub-detectors, gamma ray source distribution can be reconstructed [23][11].

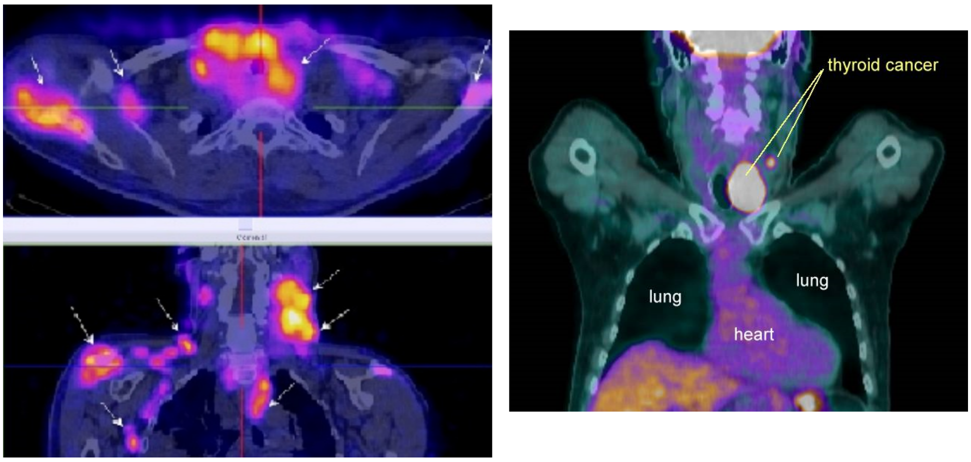

Figure 2.8: Image from a SPECT scan (left) and PET scan (right). Both fused with CT, sources [21], [22].

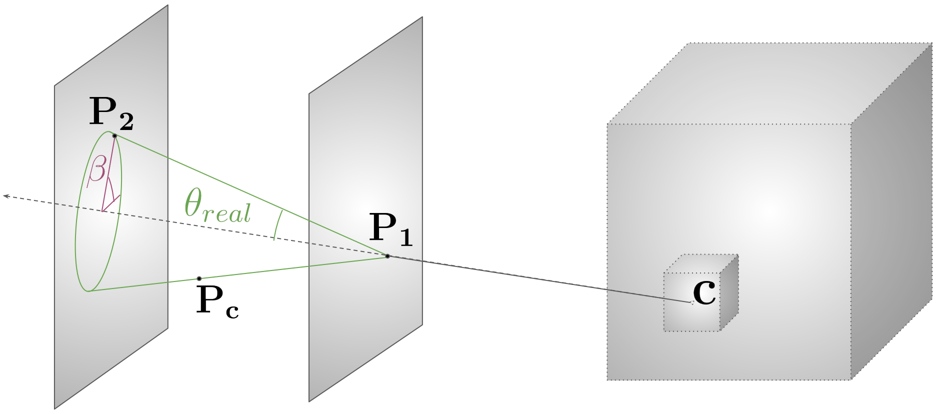

(a) : Schema of photon emission and detection.

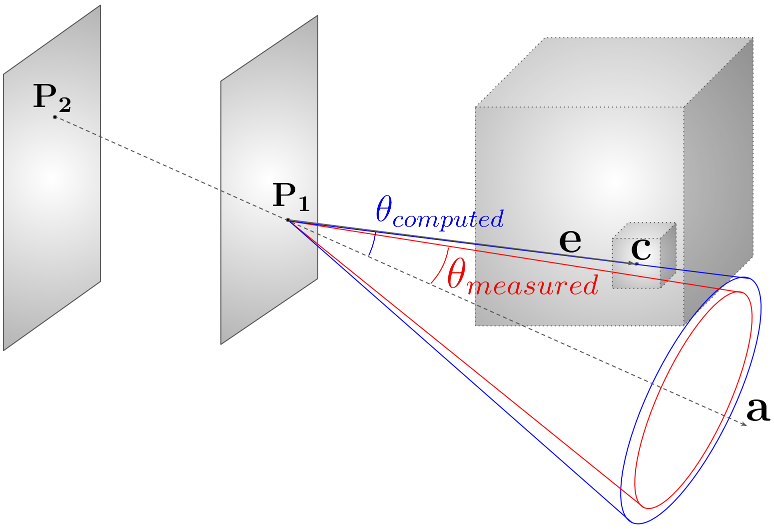

(b) : Schema of Compton reconstruction principle.

Figure 2.9: Illustrations of Compton imaging principles.

Compton imaging is based on the idea that the Compton scattering angle can be computed using measurements of the incoming photon's energy. The photon deposits part of its initial energy in the scatterer and the remaining energy in the absorber [12]. See Figure 2.9 for schema). If the detection positions on the scatterer and absorber are known, the Compton scattering angle θ can be computed using the Compton scattering formula [24]

$$\Delta\lambda = \lambda' - \lambda = \frac{h}{m_e c}(1 - \cos\theta) \tag{2.1}$$

which can be rearranged as

$$\theta = \arccos\left[1 - m_e c^2 (\frac{1}{E_0} - \frac{1}{E_1})\right] \tag{2.2}$$

where E_0 is the energy of the initial photon, E_1 is the energy of the scattered photon, m_e is the electron's mass, and c is the speed of light in a vacuum.

From the perspective of the reconstruction, the Equation 2.3.4 constrains the direction from which the photon originated to a conical shape known as the Compton cone, with the apex at the scattering detection point. The cone's central axis is the line that connects the positions of the absorption and scattering detections. The half-apex angle of the cone corresponds to the scattering angle.

When the Compton camera records a series of such incidents, referred to as Compton events, it becomes possible to reconstruct the spatial distribution of the gamma source [25].

It is important to note, that the Compton scattering formula holds if the photon interacts with an electron at rest. This assumption is often violated in real scenarios, resulting in the so-called Doppler broadening effect [11].

Klein-Nishina formula

The Klein-Nishina formula is a mathematical equation that quantifies the likelihood of a Compton scattering at a specific angle while considering relativistic effects and adhering to the principles of energy and momentum conservation. The formula (Equation 2.3) computes the differential cross section, that is proportional to the probability density, given the initial energy of the incident photon E_0, the energy of the scattered photon E_1, and the scattering angle θ. Figure 2.10 presents probability distributions for different energy levels of E_0.

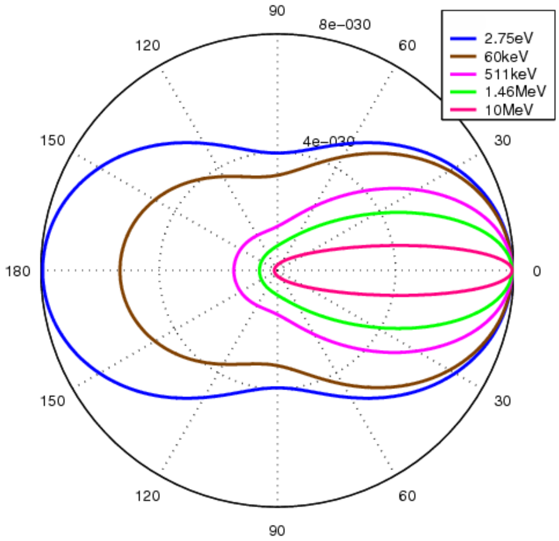

Figure 2.10: Klein-Nishina distribution for given photon energies, source [26]. The graph expresses the probability of Compton scattering under different angles given different initial energies (in color).

$$\frac{\mathrm{d}\sigma}{\mathrm{d}\Omega} = \frac{r_e^2}{2}\left(\frac{E_1}{E_0}\right)^2\left[\frac{E_1}{E_0} + \frac{E_0}{E_1} - \sin^2\theta\right] \tag{2.3}$$

Poisson distribution

Poisson distribution is a discrete probability distribution that describes the probability that exactly k events will occur in some given time period. It is a vital distribution for Compton reconstruction as it governs the radioactive decay. The expected number of decays is given by the parameter λ, which is non-negative and integer-valued. The probability mass function is defined as:

$$\Pr(X = k) = e^{-\lambda} \cdot \frac{\lambda^k}{k!} \tag{2.4}$$

Applications of Compton cameras

The Compton camera concept was initially proposed by Schonfelder in 1973 for applications in high-energy astrophysics [27]. Since then, Compton cameras have been employed on satellites and spacecraft to observe near and far space

[13] [12].

Following the 2011 Tōhoku earthquake and tsunami and the subsequent Fukushima Daiichi Nuclear Power Plant disaster, Compton cameras have been built to survey for radiation contamination in Japan and the USA [28] [13]. Application in homeland security was proposed in the UK [29].

Usage of Compton cameras in the medical field was pioneerd by Todd et al. in 1974 [30]. Over the past decade, Compton cameras have emerged as potential substitutes for mechanically collimated SPECT systems in nuclear medical imaging. Compton cameras offer the potential to work with high-energy traces and can measure multiple radiopharmaceuticals simultaneously. Nonetheless, applications remain confined to preclinical research at this stage [12]. Another recent medical application involves using Compton cameras in hadron therapy for real-time monitoring of the particle beam range during treatment [12][25].

ThyroPIX Compton camera

A research project called ThyroPIX is engaged in the development of a Compton camera for the context of thyroid cancer patients. The ThyroPIX project is supported by the Technology Agency of the Czech Republic (TACR). The members of the projects are Radalytica a.s., Advacam s.r.o., University Hospital in Motol, Czech Metrology Institute and The Center for Advanced Preclinical Imaging.

The ThyroPIX detection system is the one used in this thesis. A small and lightweight Timepix3 Compton camera is integrated into a measuring head that is attached to a collaborative robotic arm mounted on a mobile platform (Figure 2.11).

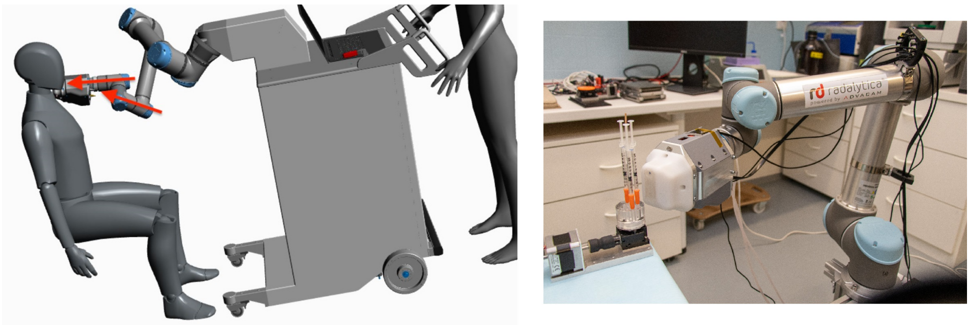

Figure 2.11: Model of the ThyroPIX system (left), current prototype version (right).

The design of ThyroPIX ensures the device's high portability and enables patient in-room measurements during radiopharmaceutical treatment. The final camera could potentialy serve as an effective alternative to the SPECT cameras and provide vital information about the progress of the treatment enabling the usage of personalised dosage.

The Compton detection module comprises a 1 mm thick square shaped scatterer layer made of Si and a 1 mm thick square shaped absorber layer made of CdTe. A distance of 20 mm separates the layers (see Figure). Each detector has 256x256 pixels with a pixel size of 55 μm. Timepix3 records time-of-arrival and energy of the gamma-ray with high precision (time resolution 1.6 ns; energy resolution 7 keV at 356 keV). The system is capable of processing up to 80 Mhits/cm^2/s.

The ThyroPIX detector automatically processes the raw acquired data (with interaction positions and energies) and outputs the cone parametrization (Equation 3.1).

Chapter 3

Simulators and datasets

3.1 Notation introduction

We have a volume in space represented by a uniform voxel grid V with a defined origin, dimensions and voxel size. Each voxel j has defined center point $\mathbf{c} = \begin{bmatrix} c_x & c_y & c_z \end{bmatrix}^T$.

Furthermore, we have a detector system comprising of two identical rectangle detectors, a scatterer and an absorber. Scatterer's position is defined by its centre point $\mathbf{S}_{\text{center}}$, its corner point $\mathbf{S}_{corner}$, two side vectors $\mathbf{s}_1$ and $\mathbf{s}_2$ and a normal vector $\mathbf{n}$. The absorber has the same size and normal as the first one, but is shifted by distance s_d behind the first detector's plane. See Figures 3.1 and 2.9 for a schema.

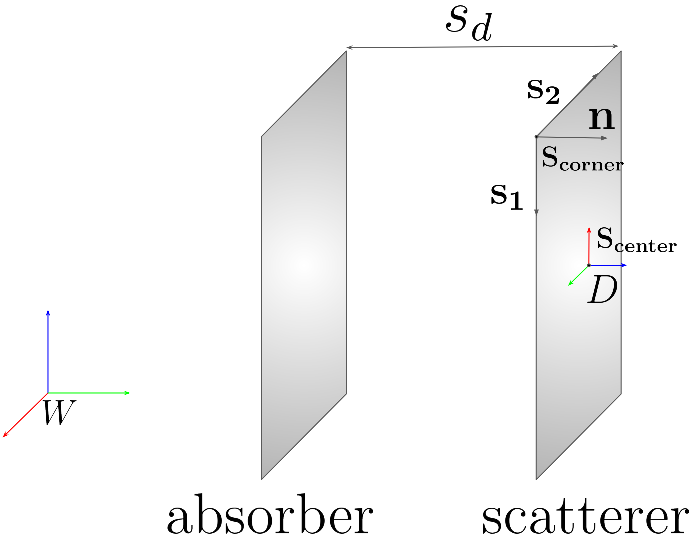

Figure 3.1: Scheme of the detector's geometry and used notation.

In the voxel grid V we have a distributed source emitting photons of known energy E_0. A photon originating from the center of a voxel j with coordinates $\mathbf{c}$ may head towards a detector system called a Compton scattering detector.

When the photon hits the scatterer at point $\mathbf{P_1}$, it undergoes Compton scattering, being scattered with an angle θ_{real}. The photon then continues with the decreased energy E_1 until it reaches a point $\mathbf{P_2}$ on the absorber where it is absorbed using the photoelectric effect. This interaction of the photon with the detector system is called a (Compton) event.

For the reconstruction, there are two related frames of reference - one is the frame of reference of the scatterer D with the origin at $\mathbf{S}_{\text{center}}$, x-axis aligned with $-\mathbf{s}_1$, y-axis aligned with $-\mathbf{s}_2$, z-axis aligned with normal vector n. The other frame of reference is the world reference frame W. The detector's frame of reference D is defined using a pose vector

$$\mathbf{pose}_D = \begin{bmatrix} S_{\text{center}_x} & S_{\text{center}_y} & S_{\text{center}_z} & \alpha & \beta & \gamma \end{bmatrix}^T \tag{3.1}$$

where the first three elements are the coordinates of the center of the first detector in the world reference frame W and the last three coordinates are the Euler angles (Z-Y-X notation) that correspond to the rotation of the robot with reference to the three axis of the world frame. The voxel centers coordinates are also in the world reference frame.

Each measured Compton event i is defined by the cone parameters given in the scatterer's reference frame D. The cone's parameters are:

$$\mathbf{event}_i = \begin{bmatrix} P_{1x}^D & P_{1y}^D & P_{1z}^D & a_x & a_y & a_z & \theta_{measured} \end{bmatrix}^T \tag{3.2}$$

where the first three elements are the coordinates of the cone apex in the reference frame of the detector, the next three elements are the coordinates of the cone axis vector $\mathbf{a} = \mathbf{P}_1 - \mathbf{P}_2$ and the last element is the measured scattering angle.

3.2 Compton simulators

A crucial role in the development, testing, and validation of algorithms and techniques for Compton imaging systems play simulators. Mainly based on the Monte Carlo principle, simulators are tools that can generate synthetic data, model detector response and validate reconstruction algorithms before being deployed in the real world.

3.2.1 Review of existing simulators

An example of such a simulator is the Geant4 toolkit [31], developed by CERN. It is an advanced general-purpose Monte Carlo simulation platform for particle transport in matter, widely used in high-energy physics, astrophysics, and radiation protection. An open-source module called GATE [32] has been developed for Geant4 to accommodate the needs of medical image reconstruction. GATE is a robust simulator, that enables realistic physics modelling and complex experimental settings. However, it has a steep learning curve and therefore its usage was outside of the scope of this thesis.

Another available simulator is the Compton Camera Simulator (CoCam Sim) developed by Advacam s.r.o.. It is a Monte Carlo simulator that allows to generate simulation data from sources of different geometrical primitives. CoCam Sim consideres a smaller subset of the physics modelling than GATE - probability of Compton scattering and photoelectric absorbtion including the interaction point, Klein-Nishina distribution of the scattering angle and attenuation coefficient inside of the detector. Furthermore, it takes into account specific detection probablities of the Timepix3 detection materials (Si and CdTe). The CoCam Sim therefore presents a very good tool for validation of the developed reconstruction methods. The disadvantage of the simulation is a relatively naive implementation in Python - point-source simulation of 10^6 photons took on average 41 seconds (wall time) - along with the limited detector geometry customizability. CoCam Sim allows sampling only at predefined locations. These are limiting factors in case of generating complex experimental scenarios or in scenarios with high number of events.

3.3 Development of custom simulator

To test the reconstruction methods, generate high volumes of sample data and complex scenarios, a simulator was developed as part of this thesis. The task was to design a Monte Carlo algorithm that performs photon tracing simulation, specifically considering Compton scattering. The simulation algorithm implements a simplification of the detection process, with the level of simplification chosen to match the model used in the reconstruction (described further). The following section describe the individual components of the developed solution.

Uniform sampling of directions of emitted photons

First task is to uniformly sample directions in which the photons exit given point source located at the voxel center $\mathbf{c}_j$. A simple uniform generation of two spherical angles θ and ϕ would result in uneven distribution of the final directions, with pole regions having more samples than equatorial areas.

Therefore, a review of available sampling methods was done and approach by Simon [33] was adopted. It uses inverse transform sampling that leads to the set of equations:

$$\begin{aligned} u &\sim U(0,1) \\ \theta &= 2\pi u \\ \phi &= \arccos(1-2u) \\ e_x &= \sin(\phi)\cos(\theta) \\ e_y &= \sin(\phi)\sin(\theta) \\ e_z &= \cos(\phi) \\ \mathbf{e} &= \begin{bmatrix} e_x & e_y & e_z \end{bmatrix}^T \end{aligned} \tag{3.3}$$

By uniformly sampling u, randomly sampled emission vectors $\mathbf{e}$ can be obtained.

Raytracing and finding intersection with the first (front) detector

Once the voxel center $\mathbf{c}_j$ and the direction of the emitted photon $\mathbf{e}$ are defined, we can find the intersection with the first detector. This can be done using linear algebra. We first find if the photon intersects the detector's plane and if so, we find if it intersects the rectangular detector. For simplification, we asume that the interaction probablity is 1 regardless of the path of the photon (incident photon will always interact).

Intersection with the detector's plane

Intersection occurs when

$$\mathbf{e} \cdot \mathbf{n} < 0 \tag{3.4}$$

The intersection point $\mathbf{P}_1$ then lies on a line parameterized by

$$\mathbf{P}_1 = \mathbf{c}_j + a\mathbf{e} \tag{3.5}$$

where $a \in \mathbb{R}$ is an unknown parameter.
Because it must hold that $\mathbf{S}\vec{\mathbf{P}}_1 \cdot \mathbf{n} = 0$ it must also hold that

$$(\mathbf{c}_j\vec{\mathbf{P}}_1 - \mathbf{c}_j\vec{\mathbf{S}}) \cdot \mathbf{n} = 0 \tag{3.6}$$

which can be rewritten as

$$\begin{aligned} ((\mathbf{P}_1 - \mathbf{c}_j) - (\mathbf{S} - \mathbf{c}_j)) \cdot \mathbf{n} &= 0 \\ ((a\mathbf{e}) - (\mathbf{S} - \mathbf{c}_j)) \cdot \mathbf{n} &= 0 \\ a &= \frac{(\mathbf{S} - \mathbf{c}_j) \cdot \mathbf{n}}{\mathbf{e} \cdot \mathbf{n}} \end{aligned} \tag{3.7}$$

Substituting the computed value of a into the parameterized line's equation then leads to the intersection point $\mathbf{P}_1$.

Intersection with the rectangular detector

To decide whether the intersection point $\mathbf{P}_1$ is inside the rectangular detector's space, we have to project the vector $\vec{\mathbf{SP}}_1$ onto the side vectors $\mathbf{s}_1$ and $\mathbf{s}_2$

$$\begin{aligned} \mathbf{s}_{1p} &= \frac{(\mathbf{P}_1 - \mathbf{S}) \cdot \mathbf{s}_1}{||\mathbf{s}_1||} \\ \mathbf{s}_{2p} &= \frac{(\mathbf{P}_1 - \mathbf{S}) \cdot \mathbf{s}_2}{||\mathbf{s}_2||} \end{aligned} \tag{3.8}$$

The intersection point $\mathbf{P}_1$ is inside the rectangular detector's space if

$$\begin{aligned} 0 \leq ||\mathbf{s}_{1p}|| \leq ||\mathbf{s}_1|| \\ 0 \leq ||\mathbf{s}_{2p}|| \leq ||\mathbf{s}_2|| \end{aligned} \tag{3.9}$$

Path from the first to the second detector

On the subset of photons that hit the first detector, we have to simulate Compton scattering and follow their new scattered path.

Sampling the scattering angle θ_{real}

Given initial energy of photon E_0, the differential cross section of scattering angle θ_{real} is given by Klein-Nishina formula. To sample angles according to the Klein-Nishina distribution, an approach using the inverse cumulative distribution function was adopted.

The idea is to uniformly sample N angles θ_{real}, find their corresponding probabilities using the Klein-Nishina formula and compute cumulative sums of the probabilities. The resulting vector is the discretized inverse cumulative distribution function with uneven step-size. To account for that, cubical interpolation is used to create even spacing between the samples. This procedure needs to be done once and the resulting vector can be saved. In the runtime, a uniform random sample is taken, multiplied by N, rounded and the result is used to index the saved vector of angles.

Sampling the emitting direction of the scattered photon

We have a point $\mathbf{P}_1$, a direction vector $\mathbf{e}$ and a scattering angle θ_{real}. We want to find all vectors $\mathbf{e}_s$ with a fixed angle from vector $\mathbf{e}$ and sample one of them. There is a cone of possible solutions.

Assuming $\mathbf{e}_s$ is a unit vector, we can construct a plane perpendicular to $\mathbf{e}_s$ at $\mathbf{P}_1 + \mathbf{e}_s$. The cone intersects this plane at a circle of radius $r = \tan(\alpha)$ centered at $\mathbf{P}_1 + \mathbf{e}_s$

The cone points can be described by

$$\mathbf{P}_c = (\mathbf{P}_1 + \mathbf{e}_s) + r\mathbf{v} \tag{3.10}$$

where $\mathbf{v}$ is a unit vector perpendicular to $\mathbf{e}_s$

The vector $\mathbf{v}$ can be decomposed into two vectors $\mathbf{v}_1$ and $\mathbf{v}_2$.

$$\mathbf{v} = \cos(\psi)\mathbf{v}_1 + \sin(\psi)\mathbf{v}_2 \tag{3.11}$$

given angle ψ.

By picking $\mathbf{v}_1$ and $\mathbf{v}_2$ to be orthogonal and selecting ψ, we obtain the vector $\mathbf{v}$.

This creates the final parametrization of the cone

$$\mathbf{P}_c = t(\mathbf{P}_1 + \mathbf{e}_s) + \tan(\theta_{\text{real}})(\cos(\psi)\mathbf{v}_1 + \sin(\psi)\mathbf{v}_2) \tag{3.12}$$

where $t \in \mathbb{R}$, $\psi \in [0, 2\pi]$

A single sample is found after sampling ψ uniformly

$$\psi \sim U(0, 2\pi) \tag{3.13}$$

generating $\mathbf{v}_1$ and $\mathbf{v}_2$ using projection and plugging it into the final parametrization equation (3.3).

Finding the intersection on the second detector

Finding the intersection with the second detector is now straightforward. We find the intersection applying the same procedure as when finding the intersection with the first detector (Section 3.3).

The resulting cone apex is the point $\mathbf{P}_1$, the cone axis is given by $\mathbf{P}_c - \mathbf{P}_1$ and scattering angle θ_{real}.

Optimization of the algorithm

To speed up the computation, the solution was implemented in the matrix form (utilizing PyTorch library), processing multiple photons at once, resulting in a fast performance. A point-source with 10^6 photons was simulated in 0.16 seconds (wall time), compared to CoCam Sim's 41 seconds on a standard PC. Thanks to the implementation in PyTorch, the simulator could also be run on GPU, further increasing the performance boost. The proposed simulator also allows a configuration in terms of source location and shape, detection poses, number of generated events, uncertainty in the scattering angle (using Gaussian noise) and random coincidences generation.

3.4 Dataset

A dataset serves as the foundation for model development and evaluation. As the reconstruction problem is very specific, there are no generally available datasets. Therefore, a custom dataset was compiled using simulators and real laboratory measurements. The design of the data was chosen to validate the reconstruction methods as well as to reflect the anatomical properties of the thyroid examination.

3.4.1 Simulated data

Own simulator

The developed simulator was used heavily to generate scenarios with different geometrical primitives. In total, around 150 scenarios were generated. The simulated shapes include spheres, elipsoids, cylinders, cones, crosses and rectangles in different configurations. The sensing locations vary from a single projection to scenarios with complex projection setup. Different sizes of the voxel grid and distances from the center of the voxel grid were considered. For some shapes, scenarios with noise in the scattering angle or with random events were generated. A sample of the generated scenarios is available in Figure 3.4.1.

CoCam Sim

The CoCam Sim was used for the validation of reconstruction methods using a more complex underlying physics model. The available shapes included a similar geometrical primitive set as the proposed simulator. The scenarios generated using CoCam Sim had a smaller number of generated events and limited sensing locations, due to the nature of the simulator.

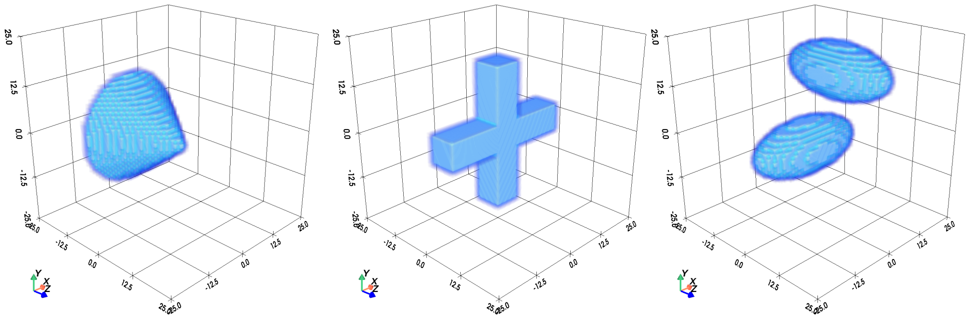

Figure 3.2: Sample images of the generated data.

3.4.2 Experimental measurements

Thanks to the ThyroPIX project, the organization of real measurements was possible.

The first experiment took place at the Department of Nuclear Medicine and Endocrinology, 2nd Medical Faculty, Charles University and University Hospital Motol. The experiment sample consisted of four ^{131}I capsules placed on two concentric cylinders (Figure 3.3). The size of the capsules was 16x7 mm. Two capsules had an activity of 25 MBq, one activity of 12 MBq and one 7.5 Mbq. The measurement was done on a rotating table, scanning a full 360 degrees turn with a step of 5 degrees (72 projections in total). The distance from the axis of rotation was 73 mm. The number of Compton events acquired was 46 685.

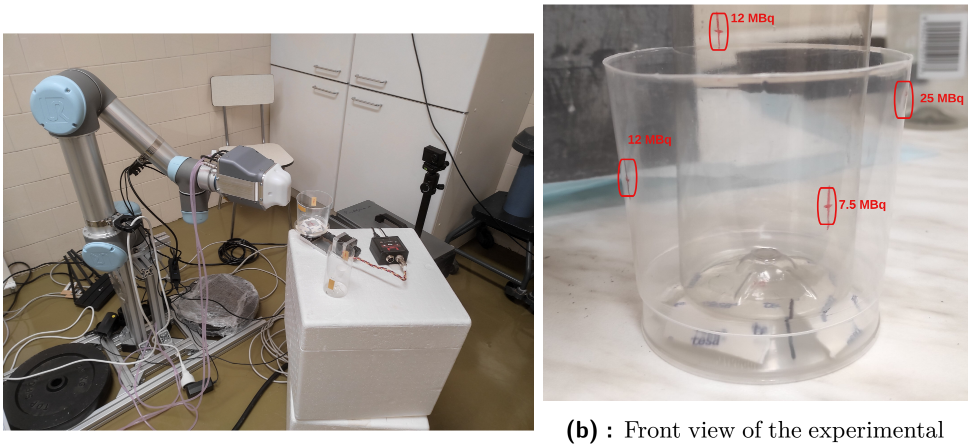

(a) : Measurement setup, with the phantom in front of the detector.

(b) : Front view of the experimental sample with marked locations and activities of the capsules.

Figure 3.3: Overview of the concentric cylinder phantom (without the capsules).

The second experiment utilized an anthropomorphic human phantom with a neck insert containing three capsules (16x7 cm) of ^{131}I (63 MBq, 33 MBq and 23 MBq). The phantom was developed by the Czech Metrology Institute, using a special material that provides similar properties as human tissue. The capsules were fitted into the insert and then bathed in a gel-like solution. The measurements were done using the ThyroPIX robotic prototype system, acquiring data from 21 sensing locations that imitated a very restrictive medical examination scenario (horizontal range of 70°, vertical range of 25°). Using the same sensing locations, the insert was firstly measured inside of the human phantom and then standalone, obtaining 40 406 and 81 505 events, respectively.

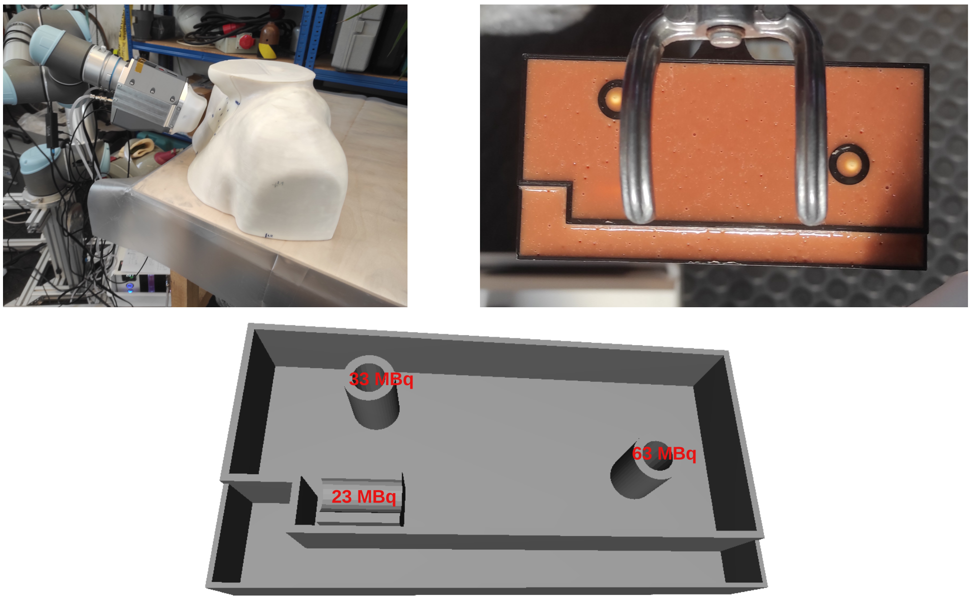

Figure 3.4: Overview of the anthropomorphic human phantom.

Clinical data from patients were unfortunately not acquired in the time of this thesis due to the complexity of clinical trial approval, but are scheduled later this year.

3.5 Data preprocessing

As the input data were obtained in multiple sensing locations and coordinates are in the reference frame of the detectors, preprocessing was done on the input data to transform the coordinates into the world coordinate frame.

Given the detector pose from Equation 3.1, the transformation from detector's reference frame D into world reference frame W can be formulated as a rigid transformation and computed using the rotation matrix

$$\begin{aligned}
\mathbf{R} &= \mathbf{R_z}(\alpha) \cdot \mathbf{R_y}(\beta) \cdot \mathbf{R_x}(\gamma) \\
&= \begin{bmatrix} \cos(\alpha) & -\sin(\alpha) & 0 \\ \sin(\alpha) & \cos(\alpha) & 0 \\ 0 & 0 & 1 \end{bmatrix} \cdot \begin{bmatrix} \cos(\beta) & 0 & \sin(\beta) \\ 0 & 1 & 0 \\ -\sin(\beta) & 0 & \cos(\beta) \end{bmatrix} \cdot \begin{bmatrix} 1 & 0 & 0 \\ 0 & \cos(\gamma) & -\sin(\gamma) \\ 0 & \sin(\gamma) & \cos(\gamma) \end{bmatrix} \\
\mathbf{t} &= \mathbf{S}_{\text{center}}
\end{aligned} \tag{3.14}$$

The coordinates of the cone parameters in the coordinate frame of the detector D are then transformed into the coordinates in the world reference frame W using a simple transformation

$$\begin{aligned}
\mathbf{P}_1^W &= \mathbf{R} \cdot \mathbf{P}_1^D + \mathbf{t} \\
\mathbf{a}^W &= \mathbf{R} \cdot \mathbf{a}^D
\end{aligned} \tag{3.15}$$

In the following parts of the thesis, the cone parameters are always assumed to be in the world reference frame W, and the reference frame index is omitted.

Chapter 4

Reconstruction methods overview

Medical image reconstruction algorithms convert raw data acquired from various imaging modalities into high-quality, interpretable images that assist clinicians in the diagnostics of various medical conditions. In contrast to PET/SPECT, the Compton camera provides information about the scattering angles of individual photons. This allows us to obtain higher detection efficiency (up to two orders of magnitude [34]), but at the expense of a complex image reconstruction process. Whereas PET/SPECT associates each photon with a line (2 DOF), Compton imaging links measurement events to a cone surface (5 DOF), implying a more ill-conditioned problem. The size and mutual arrangement of the scatterer and the absorber can also non-trivially affect the probability of detection [35].

For the reasons mentioned above, traditional PET/SPECT reconstruction methods are not applicable for the Compton camera system. Although it's theoretically possible to formulate the Compton reconstruction methods in a similar manner, the difference in the dimensionality of the projection operator presents a significant difference. In Compton imaging, we're unable to capture, store, or process the projections and are instead compelled to operate exclusively with a discrete list of detections, referred to as list-mode.

4.1 List-mode

List-mode presents a data processing approach that is needed in Compton reconstruction. While PET/SPECT utilizes bins - discrete intervals used to organize, aggregate and represent individual events. In the list-mode approach, the size of the bins is reduced so that at most one event is in each bin and bins with zero events are ignored - adopting the list-mode approach. In the context of Compton reconstruction, the list-mode method works with coincidence lists containing parameters of every event (cone apex position, cone axis, scattering angle). This approach avoids binning and associated quantization problems while maintaining reasonable memory requirements [35]. To generate list-mode data, the detection system must be event-based rather than pixel-based – meaning it must contain fast read-out electronics and memory to give information about every incoming photon [16]. Reconstruction methods then work with individual events as opposed to collections of events (bins) in SPECT/PET.

4.2 Forward projection

Classical approaches to image reconstruction are mainly based on the so-called forward and backward projection operators. Forward projection is a mathematical process that computes individual projections of an unknown image function [35].

In traditional PET/SPECT reconstruction methods, this process is done using Radon transform, a linear transformation that converts the unknown image function μ (assumed to be proportional to the radioisotope source densities) into the projection function $R\mu$ using a line kernel. The projection function $R\mu$ is parametrised by pixel index and angular orientation of the detector. Radon transformation can be represented as an integral or as a dot product. Albeit the Radon transform is defined for the continuous case, it is in practice often discretized. The linearity of Radon transform is very convenient as the Radon transform of the entire volume is the sum of Radon transforms of the individual points [16].

In case of Compton imaging, line kernel must be replaced by a conic kernel and direct standard Radon transformation cannot be used. The detection itself is a stochastical process and forward projection is better formulated as a probability distribution over events. For some restrictive cases, projections can be computed using conical Radon transform [36], however there is no analytical solution for the general case.

To illustrate the concept of Radon transform, let us consider a simple 2D case. We introduce an unknown image function of two variables $\mu(\mathbf{x})$ that represents the photon density - estimated number of photons emitted in at point $\mathbf{x}$. The projection function p is the Radon transform of function μ and is defined as

$$p(\boldsymbol{\tau}) = R\mu(\boldsymbol{\tau}) = \int_{\xi} \mu(\mathbf{x})\, dx \tag{4.1}$$

where $\boldsymbol{\tau}$ is the parametrisation of the projection and the integral is taken with respect to the kernel ξ - in case of PET/SPECT a line (Figure 4.1), in case of Compton imaging a cone.

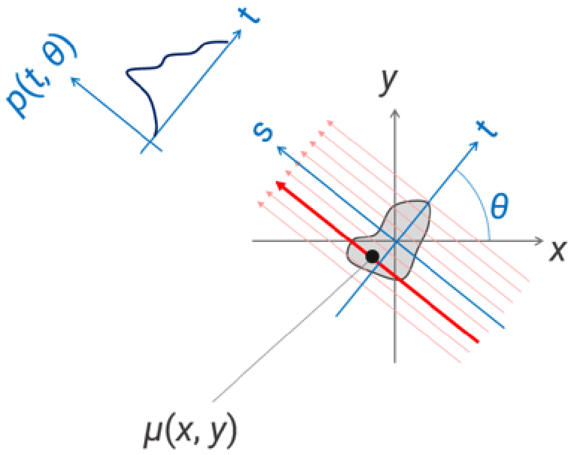

Figure 4.1: Principle of a Radon transform, source [37].

Reconstruction

The task of image reconstruction is to approximate the inverse of the forward operator. Given one or more projection functions p, the goal is to compute the unknown image function μ, from which the projections originated.

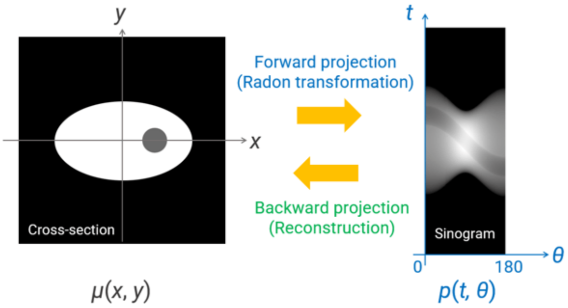

Figure 4.2: Basic scheme of image reconstruction, source [37].

4.3 Backprojection

Backprojection is the dual operator to the forward projection (Figure 4.2). It takes the projection data from the detector space (cone parameters) and distributes it back into the image space.

For PET/SPECT, this procedure is formulated as a sum across all available projections (Figure 4.3).

$$\mu(\mathbf{x}) \approx \eta \sum_{i=1}^{N} p(\mathbf{x}) \tag{4.2}$$

where η is a normalization factor, in case of Compton data $\frac{1}{N}$

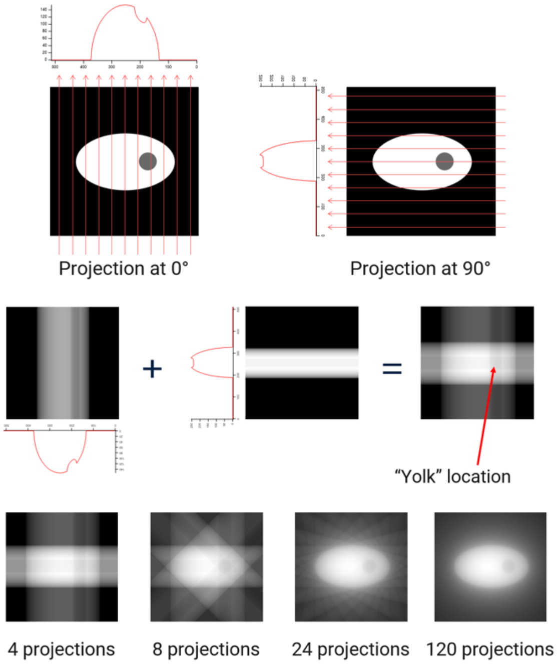

Figure 4.3: Principle of the backprojection method, source [37].

In case of Compton reconstruction, each measured event corresponds to a cone surface distribution. These distributions are projected on the voxel grid and superimposed.

4.4 Filtered backprojection

As stated in the previous section, naive backprojection superimposes available projections.

In the case of an line projection setup (PET/SPECT), these projections overlap more in the center of the volume than on the boundaries. To correct for this factor, filtered-backprojection proposes to apply a convolution to the projection data using a filter kernel. An ideal filter would be in the form of $|\omega|$. However, due to the presence of high-frequency noise, modifications such as the Ram-Lak filter (Equation 4.3) are often used [38].

$$H(\omega) = \begin{cases} |\omega|, & \text{for } |\omega| \leq \omega_c \\ 0, & \text{for } |\omega| > \omega_c \end{cases} \tag{4.3}$$

In PET/SPECT, each projection is filtered and the projections are superimposed as in the case of a simple back-projection (Figure 4.4). Even though the filtered backprojection method has underlying assumptions such as linearity of the projection operator, infinite amount of projections, continuous space, etc., it works surprisingly well even in many real-life scenarios and is broadly used [38].

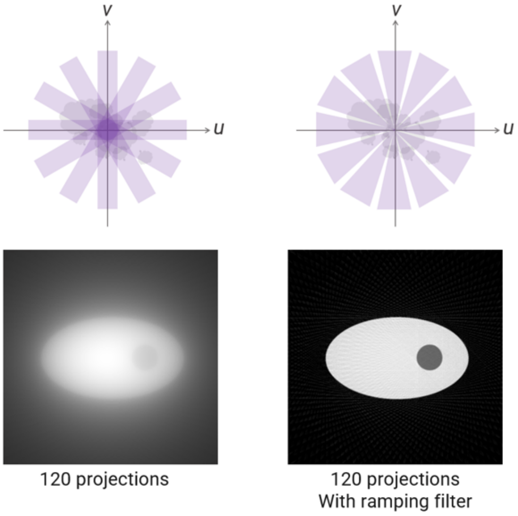

Figure 4.4: Principle of a filtered backprojection method, source [37].

In Compton imaging, the superimposed conical projections of individual events usually accumulate near the detector, but the location also depends on the particular scanning procedure and layout of the available projections. Direct application of the filtered backprojection is not possible, but there have been attempts ([39] [40]) to develop a similar procedure for the case of Compton imaging. The most widely regarded approach uses spherical harmonics [39] – it transforms the original detector's surface by moving each pixel in the centre of a unit sphere. This step allows Radon's transform to be applied, enabling a fast reconstruction. However, this approach is very sensitive to the discretization and to the number of available projections. Furthermore, normalization of the intensity values is challenging [35].

4.5 Iterative methods

The iterative methods inherently work with a discretized model, which can be modelled as a system of equations

$$\mathbf{T}x = b \tag{4.4}$$

where the unknown variables $\mathbf{x}$ are the values of the unknown source densities, which are trying to satisfy the measured projection data $\mathbf{b}$, given the discretized projection operator matrix $\mathbf{T}$. The matrix $\mathbf{T}$ is also called a system modelling matrix and describes the contribution of elements of the discretized image function to projection data.

In general, the system of equations is often overdetermined or underdetermined and cannot be solved directly. The overdetermined problem is often reformulated as minimizing the norm of the residuals

$$\min_x \|Tx - b\|, \tag{4.5}$$

the underdetermined as a regularization problem.

A direct solution is not obtainable (because of the large size of matrix **T**) and iterative methods are employed. Most methods usually start from some prior initial guess of the discretized image function. Given this guess, a set of projections is created and compared with the measured projections. The difference between these two is used to correct the estimated discretized image function. These steps are repeated until the estimate converges to an acceptable level.

4.6 Maximum-likelihood expectation-maximization (MLEM)

Maximum likelihood expectation maximization (MLEM) is an iterative statistical method that tries to find the maximum likelihood parameters of statistical models. Usually, these models include hidden (latent) variables or unobserved data points.

In the context of nuclear image reconstruction, the latent variables are the Poisson distribution parameters $\hat{\lambda}_j$, that are proportional to the concentration of the radionuclide. The task is to find the maximum likelihood parameter for each pixel/voxel.

In a general case, maximum likelihood parameters are often calculated using gradient methods by computing derivates of the likelihood function. However, when latent variables are present, the solution is either complicated to derive or non-existent. Therefore a two-step algorithm called Expectation-maximization is utilized.

The EM algorithm consists of two steps that alternate:

- E-step: Computes the expected log-likelihood given the latent model parameters $\hat{\lambda}_j$ from the previous iteration.
- M-step: Aims to find the new estimate of the $\hat{\lambda}_j$, that maximizes the conditional expectation.

When the underlying statistical model is of an exponential family, it is often possible to derive a closed-form formula for each iteration.

4.6.1 Derivation

The following section provides a derivation of MLEM for classical nuclear imaging methods (PET/SPECT) and then presents adaptation for the list-mode Compton reconstruction. In the interest of brevity and a slight abuse of notation, assume in this derivation that i denotes either a measurement bin (in context of PET/SPECT) or one Compton event (in context of Compton imaging).

Assume that the mean number of counts detected in bin i follows Poisson distribution and the probability that data from bin i originated in voxel j is denoted t_{ij}. This probability contains all physical features of the detection process and detector geometry.

The expected mean number of counts detected in bin i given Poisson parameters λ_j and probability t_{ij} is:

$$\mu_i = \sum_j t_{ij} \cdot \lambda_j \tag{4.6}$$

We introduce random Poisson variables X_{ij} and Y_i. X_{ij} represents the number of photons emitted by voxel j contributing to bin i. Y_i is the total number of photons recorded bin i, which is equal to $Y_i = \sum_j X_{ij}$. The X_{ij} consistutes the unobserved data, and Y_i is the measured number of photons.

The probability of seeing the data $y_i \sim Y_i$ given the mean value μ_i is given by

$$p(y_i|\mu_i) = e^{-\mu_i} \frac{\mu_i^{y_i}}{y_i!} = e^{-\left(\sum_j t_{ij} \cdot \lambda_j\right)} \frac{\left(\sum_j t_{ij} \cdot \lambda_j\right)^{y_i}}{y_i!} \tag{4.7}$$

Assuming the measurements are independent, the likelihood of seeing the measured data given the emission rate values $\boldsymbol{\lambda}$ is then computed as

$$L(Y|\boldsymbol{\lambda}) = \prod_{i=1}^{I} p(y_i|\mu_i) \tag{4.8}$$

The task is to maximize this likelihood with respect to $\boldsymbol{\lambda}$. In practice, maximizing the likelihood L is often replaced by maximizing the log-likelihood $log(L)$. We first express this log-likelihood as

$$\begin{aligned}\log(L(Y|\boldsymbol{\lambda})) = \log\left(\prod_{i=1}^{n} p(y_i|m_i)\right) &= \sum_{i=1}^{n} \log\left(p(y_i|m_i)\right) = \\ &= \sum_{i=1}^{n} \left(-\mu_i + y_i \log(\mu_i) - \log(y_i!)\right) = \\ &= \sum_{i=1}^{n} \left(-\left(\sum_j t_{ij} \cdot \lambda_j\right) + y_i \log(\left(\sum_j t_{ij} \cdot \lambda_j\right)) - \log(y_i!)\right)\end{aligned} \tag{4.9}$$

.

It is impossible to derive the closed-form solution and we have to resort to the EM algorithm instead.

The goal of the E-step is to determine the conditional expectation of the likelihood given the measurements and the estimate $\hat{\boldsymbol{\lambda}}$. Following the derivation of Lange et al. [41], after neglecting the term $\log(y_i!)$, the conditional expectation is

$$\mathbb{E}(\log(L(Y|\boldsymbol{\lambda}))|\hat{\boldsymbol{\lambda}}) = \frac{t_{ij}\hat{\lambda}_j^l}{\sum_k t_{ik}\hat{\lambda}_k^l} \tag{4.10}$$

The M-step follows from that and determines the new estimate $\hat{\lambda}$ that maximizes the conditional expectation.

$$\frac{\partial}{\partial\hat{\lambda}}\mathbb{E}(\log(L(Y|\boldsymbol{\lambda}))|\hat{\boldsymbol{\lambda}}) = 0 \tag{4.11}$$

Solving this equation gives the final update formula.

$$\hat{\lambda}_j^{l+1} = \frac{\hat{\lambda}_j^l}{s_j}\sum_i \frac{t_{ij}y_i}{\sum_k t_{ik}\hat{\lambda}_k^l} \tag{4.12}$$

where s_j is the probability of detecting a photon from voxel j calculated across all projections $s_j = \sum_i t_{ij}$.

When using list-mode data in Compton imaging, we consider each event i separately (notice the change in notation). Consequently, the Equation 4.12 has to be modified. Firstly, the term y_i has only binary values and can be excluded, summing only over measured events. Furthermore, due to the inability to compute t_{ij} for all possible Compton events i, it is no more possible to compute $s_j = \sum_i t_{ij}$ and separate models must be derived for the computation of this term. The initial estimate of λ_j values can be uniform or obtained using backprojection [42]. The final LM-MLEM formula for the application in Compton imaging has the form:

$$\hat{\lambda}_j^{l+1} = \frac{\hat{\lambda}_j^l}{s_j} \sum_i \frac{t_{ij}}{\sum_k t_{ik} \hat{\lambda}_k^l} \tag{4.13}$$

Given a non-negative estimate, the formula guarantees the non-negativity of the solution.

System modelling

Elements t_{ij} are called system modelling factors or a system matrix elements (although the system matrix itself can be constructed only for PET/SPECT). They represent the probability that a photon emitted from voxel j will be detected as event i. The system modelling factors account for the Compton detection process and play a significant role in the final resolution of reconstructed images. Currently, there is no established model for the calculation of the system model. A few models have been reported in the literature for some cases [11], and others use Monte-Carlo simulations for the detection process and the behaviour of detector devices [34].

Sensitivity modelling

Elements s_j are called sensitivity factors. They represent the probability that a photon emitted from voxel j will be detected during the entire scanning procedure. Sensitivity can be understood as a correcting factor that accounts for not all voxels being scanned from the same angle and distance. Sensitivity is the sum of a subset of system modelling matrix $s_j = \sum_i t_{ij}$. With binned data (PET/SPECT), the system elements for all possible detections can be quantified and summed. When using a list-mode approach, system matrix elemenents are calculated only for a small number of detections and sensitvity must be modelled using alternative methods.

Properties of MLEM

Introduced by Lange and Carson in 1984 [41], the MLEM algorithm is widely regarded as a standard method in Compton imaging.

The advantage of the MLEM algorithm is the ability to model and compensate for a wide range of phenomena present in the detection process. However, its high computational complexity (rooted in the computation of the system matrix factors) hinders widespread use. Code must be optimized and some modelling factors must be neglected to obtain reasonable time performance

[35] [42]. Furthermore, the algorithm guarantees converges only to a local optimum, and the convergence rate cannot be bounded [43]. In practise, the statistical noise and the ill-conditioned nature of the problem may lead to significant noise in the reconstructed images. As a consequence, the iterations of the MLEM algorithm have to be stopped at some point [13].

4.7 MAP

The MAP (Maximum A Posteriori) algorithm is an extension of the MLEM algorithm based on the Bayesian estimation principle. The objective is to maximize the posterior probability function, given the measured data and some prior information or constraints, such as smoothness or continuity.

$$\boldsymbol{\lambda}^* = \arg\max_{\boldsymbol{\lambda}} (L(Y|\boldsymbol{\lambda}) \cdot P(\boldsymbol{\lambda})) \tag{4.14}$$

MAP can be understood as a MLEM with incorporated regularization. The regularization can incorporate assumptions about the source's spatial distribution, such as penalization for changes between neighbouring pixels (ex. convex non-quadratic smoothing prior). Such an approach usually results in smoother images with less noise and fewer artefacts, especially in low count rates, although at the cost of increased computational complexity.

MAP generally produces smoother images with lower noise levels than MLEM. However, the choice of prior information in MAP can significantly impact its performance [35].

4.7.1 Total variation

Total variation [44] presents a regularization method for noise reduction, that aims to remove noise while preserving edges. The total variation is defined as

$$TV(\lambda) = \int_V |\nabla \lambda(v)| dv. \tag{4.15}$$

The idea is to minimize the L_1-norm of the gradient in the reconstructed volume.

Minimizing total variation presents a significant challenge due to the non-smooth nature of the loss function associated with it. Achieving adequate convergence utilizing the gradient descent algorithm proves to be a difficult task. The primal-dual formulation is often employed to achieve fast convergence.

Algorithm of Fadili-Peyré [45]

It is an iterative algorithm that minimizes the total variation using a projection on the set of images whose total variation is bounded. To compute the projection, a dual formulation is used.

Algorithm of Chambolle [46]

It is an iterative algorithm that performs the minimization of the total variation using a dual formulation, in which the original problem is formulated as a discrete problem and uses a specific splitting of the energy functional to make the problem easier to solve.

Several solutions to the MAP-EM problem given total variation prior (maximum likelihood with minimum L_1-norm) were proposed in the literature for SPECT and PET reconstruction [47], [48].

4.8 Compton reconstruction state of the art

Tashima et al. [25] provided a brief summary of the history of Compton reconstruction in the medical field: Todd et al. [30] first employed the Compton camera in nuclear medicine imaging in 1974, initially using simple backprojection techniques. Throughout the 1980s and 1990s, mathematical investigations were conducted to derive analytical formulas and iterative methods. Around 2000, some progress was made in developing analytical formulas, but the primary emphasis shifted to iterative methods, specifically the Compton list-mode MLEM [41]. A few innovative methods have emerged recently, but the LM-MLEM and its variants continue to be considered the golden standard [25].

Discretization

Lojacono [11] discussed the challenge of conversion from continuous space to discrete. The team reviewed existing methods of voxel-cone intersection, dividing them into elipse stacking (slicing of volume) and ray tracing. Furthermore, Lojacono focused on the comparison of three methods called Surface of Intersection, Volume of Intersection and Center of Voxels. Lojacono concluded that the Center of Voxels approach has the advantage of being simple to implement and compute.

Method selection

Frandes et al. [35] performed a review focusing on selecting appropriate reconstruction methods for different Compton imaging applications. The researchers concluded that backprojection and MLEM are suitable methods for near-field source imaging.

MLEM

Regarding the iterative methods, Parajuli et al. [12] analyzed the MLEM method, stating that algorithms must be optimized to perform imaging at realistic times and machine specifications for each objective. According to the article, determining the correct system matrix model is essential for reconstruction accuracy.

Feng et al. [34] [13] provided an extensive study of Compton imaging. The researchers accessed the limits of the ideal Compton imaging scenario by considering a simple geometry, an ideal detection process and a monoenergetic synthetic phantom. The ideal data were produced by Monte Carlo simulation. The reconstructed volume size was 121x34x34 voxels with a spatial size of 0.253 cm^3. They tested gamma-ray energies 511 keV, 2 MeV, and 4 MeV. The team utilized both conical filtered backprojection and MLEM. Feng et al. concluded that the analytic methods are fast but work reasonably well only for a high number of events and restricted scenarios. In particular, the list-mode MLEM methods needed a range between $2 \cdot 10^4 - 10^6$ while the filtered backprojection algorithm required more (Figure 4.5). Furthermore, analytic methods could not adequately account for the detection model, statistical noise, and missing projections, giving less precise results. Regarding gamma-ray energy, the advantage of Compton cameras over standard imaging modalities is more evident at high energies where the collimators become transparent. Feng et al. stated that without regularization, the MLEM tends to diverge in practice (Figure 4.6). The reconstruction quality was assessed using the structural similarity (SSIM) index between the reconstructed image and the reference normalized to their maximum intensity. The researchers argued against optimizing the reconstruction for the smallest MSE as better uniformity in constant intensity regions could be obtained with a larger MSE.

Sakai et al., 2020 [49] introduced a median root prior OSEM algorithm to reduce noise by adding a median filter. The OSEM is an enhancement of the MLEM that is designed to improve computational efficiency [12]. The raw data are divided into subsets, reducing the amount of processing in each iteration, and updates are performed for each subset. The resulting reconstruction after each subset becomes the starting value for the next subset. Researchers state that the optimal number of iterations is not known in advance, and MLEM and OSEM are prone to amplifying the noise through

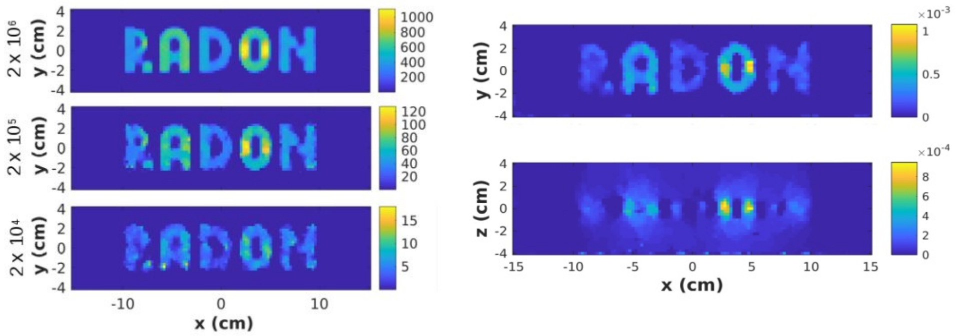

Figure 4.5: Influence of the number of Compton events on the reconstruction outcome - left: TV-MAP-EM after 200 iterations with number of events on the left; right: filtered backprojection after $1.25 \cdot 10^7$ events, source [13].

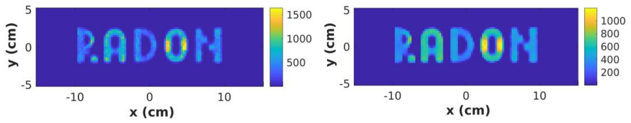

(a) MLEM, iteration 50

(b) Dual TV-MAP-EM-FISTA, iteration 50

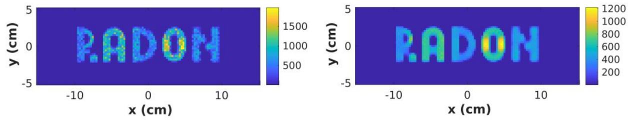

(c) MLEM, iteration 200

(d) Dual TV-MAP-EM-FISTA, iteration 200

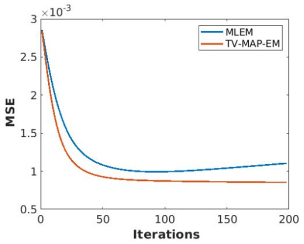

Figure 4.6: Comparison of convergence of a standard MLEM and the regularized TV-MAP-EM, source [34].

excessive iterations. Sakai et al. evaluated their reconstruction method using Monte Carlo simulations of two point sources of 511 keV gamma rays, with a separation distance ranging from 5–15 mm, using 16 000 Compton events. The algorithm reconstructed 2D images.

Alternative methods

Zhiyang et al., 2020 [50] discussed the use of a deconvolution with a point spread function, which is reportedly hard to implement because the point spread function is spatially variant. The team developed a list-mode ordered subset expectation maximization algorithm variant with the shift-variant point spread function (LM-OSEM-SV-PSFs). In their study, the SV-PSFs were derived from the Monte Carlo simulated point source measurements at various positions.

Daniel et al. [51] proposed a novel approach using an inversion method that utilizes Bayesian approach. Their solution used a single-plane pixelated miniature detector, and the results are 2D images. The algorithm works well for the 2D reconstruction of far-field sources, where it surpasses the

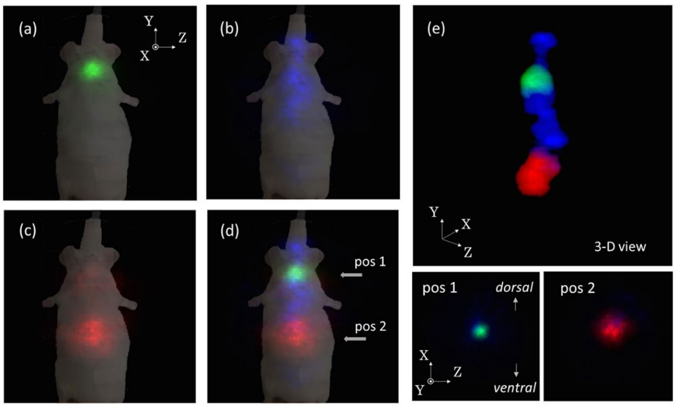

Figure 4.7: Results of Kishimoto et al., source [53].

performance of direct backprojection with slower runtime.

Andreyev et al. [52] introduced the stochastic origin ensemble (SOE) method. This algorithm is based on the Monte Carlo Markov chains and draws inspiration from the Metropolis–Hastings algorithm. Unlike other iterative methods that work with a set of voxels, SOE reconstructs a set of discrete sources and works with the origins of the measured events. SOE is mainly used in the far-field imaging of environmental sources [25] [12].

Existing medical applications

Compton imaging technology is still in the developmental stage and is not yet routinely used in clinical practice [25]. For the practical application of Compton imaging in medicine, there are challenges related to detector performance, processing hardware, and imaging algorithms [12].

In 2017, Kishimoto et al. [53] demonstrated multicolour imaging using a Compton camera prototype consisting of two scatterers and one absorber (Figure 4.7). The detector system rotated around a single axis. The team simultaneously measured three types of nuclides ^{131}I (364 keV), ^{85}Sr (514 keV), and ^{65}Zn (1116 keV). Kishimoto et al. reported that combining high-energy tracers could provide a significant clinical benefit [25]. The imaging procedure was reported to take from two to four hours.

Tashima et al. [28] developed a full-ring Compton imaging system and used it to compare the performance of the Compton camera and PET. The team conducted experiments with cylindrical, small rod phantoms filled with ^{89}Zr, which emits both 909 keV gamma rays and positron pairs. For both Compton imaging and PET, reconstruction was performed using OSEM. The researchers highlighted the significance of an accurate system response model but also noted that factors must be neglected to avoid computational complexity. The implementation of Tashima et al. required two hours for one

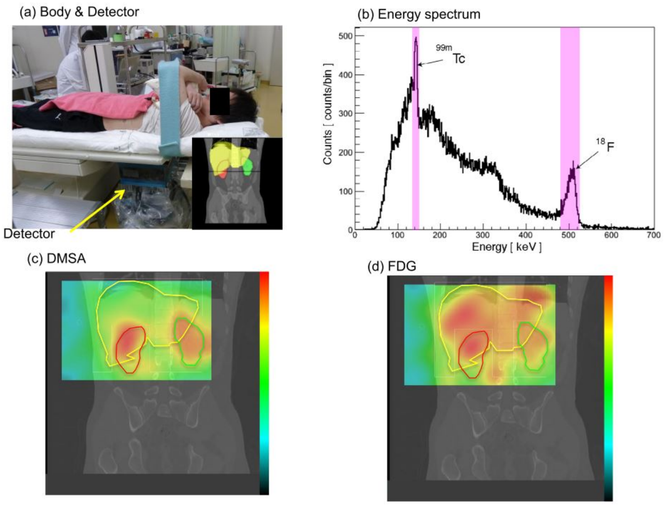

Figure 4.8: Results of Nakano et al., source [18].

iteration using two GPUs.

Hatsukawa et al. [54] performed Compton imaging with another type of Compton camera called electron-tracking Compton camera (ETCC), which utilizes a gas to track the electron detached in the Compton scattering interaction. The researchers reconstructed 2D images with the list-mode MLEM reconstruction method.

Nakano et al. [18] published a study describing the first clinical patient study, which employed Si/CdTe Compton camera for simultaneous imaging of ^{99}Tc and ^{18}F injected in a body of a human volunteer. The team presented 2D images superimposed onto CT slices (Figure 4.8).

Chapter 5

Methods

5.1 Conic projection methods

First step in the reconstruction was the construction of backward projection operator.

Approaches based on center of voxels were selected for cone projection as [11] reported this approach to show the best performance in time-constrained scenarios.

Proposed methods can be divided into distance-metric functions and error-evaluation function.

The following two distance-metric functions were proposed:

- **Angular difference**
  For each voxel j, we construct the emission vector $\mathbf{e} = \overrightarrow{\mathbf{P_1 c}}$ between the given cone apex and voxel center. Furthermore, we compute the angle $\theta_{computed}$ between the emission vector $\mathbf{e}$ and the given cone axis vector $\mathbf{a}$ and compare it to the given angle $\theta_{measured}$

$$\begin{aligned} \mathbf{e} &= \mathbf{c} - \mathbf{P_1} \\ \theta_c &= \arccos\left(\mathbf{e} \cdot \mathbf{a}\right) \\ \text{error} &= \|\theta_{measured} - \theta_{computed}\| \end{aligned} \tag{5.1}$$

- **Perpendicular distance**
  This method works by computing the perpendicular distance of a voxel center to the conic surface. The idea is to compute first the real distance to the axis of the cone and then compute the ideal distance to the axis that the surface of the cone has. These distances are then subtracted resulting in the error.

$$\begin{aligned} d_r &= \|\mathbf{e} - (\mathbf{e} \cdot \mathbf{a}) \cdot \mathbf{a}\| \\ d_i &= \|\mathbf{e} \cdot \mathbf{a} \cdot \tan\theta_m\| \\ \text{error} &= \|d_r - d_i\| \end{aligned} \tag{5.2}$$

There are two evaluation functions proposed:

- Binary step function given by

  $$\text{voxel\_increment}(\text{error}) = \begin{cases} 1 & \text{if error} < \tau \\ 0 & \text{otherwise} \end{cases} \tag{5.3}$$

  where τ is a threshold

- Normal distribution error function given by

  $$\text{voxel\_increment}(\text{error}) = \frac{1}{\sqrt{2\pi\sigma^2}} e^{-\frac{\text{error}^2}{2\sigma^2}} \tag{5.4}$$

where σ is a parametric variance

All of the proposed conic projection methods have been vectorized and will therefore be treated as vector operations in the further text.

5.2 Backprojection

Proposed implementation of backprojection works by superimposing all the measured events onto the volume V. For each event, the algorithm uses first a distance function to measure the distance between a voxel and the conic surface and then uses a evaluation function to compute the increment that the event in consideration contributes to the particular voxel.

The proposed implementation uses PyTorch functions and uses computations in matrix form. This enables to avoid computation-heavy cone-tracing algorithms and instead calculate the event increment for every voxel at once, especially if GPU is available.

The general implementation is straightforward and is described in Algorithm 1

5.3 LM-MLEM

After a thorough look at state of the art, the maximum likelihood expectation maximization was selected as a baseline method. This is due to its favourable

Algorithm 1 Backprojection

```
procedure ComputeBackprojection(list of events I, centers of voxels C)
    Initialize vector $\boldsymbol{\lambda} = 0$
    for each event $i$ do
        $\boldsymbol{\lambda}$ += EvaluationFunction(DistanceFunction($I[i]$, $C$))
    end for
return $\boldsymbol{\lambda}$
end procedure
```

properties in the near-field and convenient modeling ability. List-mode was adopted. The multiple detector poses are simply treated as more bins for the Compton data.

Naive implementation of the Equation 4.13 is presented in Algorithm 2.

Algorithm 2 LM-MLEM - naive implementation

```
procedure ComputeLM-MLEM(list of events I, centers of voxels C, detector poses D)
    $\boldsymbol{\lambda}$ = Backprojection(I, C)        ▷ Initialize vector with backprojection
    for each iteration $l$ do
        for each voxel index $j$ do
            CumSum = 0                                ▷ Set cumulative sum
            for each event $i$ do
                EventSum = 0                          ▷ Set event sum
                for each voxel index $k$ do
                    EventSum += $t_{ik}\lambda_k^l$
                end for
                $t_{ij}$ = SystemModel(i)
                CumSum += $t_{ij}$/EventSum
            end for
            $s_j$ = SensitivityModel(C,D)
            set $\lambda_j^{l+1} = \left(\lambda_j^{l+1} \cdot \text{CumSum}\right)/s[j]$
        end for
    end for
return $\boldsymbol{\lambda}$
end procedure
```

5.3.1 Computational optimization

Several improvements have been proposed to optimize the runtime and avoid unnecesary calculations.

- Sensitivity values can be precomputed, saved for each scenario and loaded during runtime.

- Given event i we can evaluate system probabilities for all voxels at once.
- Operations can be vectorized, enabling batch computation.
- If implemented correctly, the reconstruction method can be employed on GPU. In particular, the RCI cluster [55], comprising CPU and GPU nodes can be utilized. The GPU nodes consist of NVIDIA Tesla V100 with 32GB memory.

The improved LM-MLEM algorithm is presented in Algorithm 3

Algorithm 3 LM-MLEM - optimized implementation

```
procedure ComputeLM-MLEM(list of events I, centers of voxels C, detector poses D)
    $\boldsymbol{\lambda}$ = Backprojection(I, C)    ▷ Initialize values with backprojection
    $\mathbf{s}$ = SensitivityModel(C, D)    ▷ Precompute sensitivity
    for each iteration $l$ do
        $\boldsymbol{\lambda}_{increment} = 0$    ▷ Initialize iteration increment
        for each event $i$ do
            $\mathbf{t_i}$ = SystemModel(i)
            $d = \mathbf{t_i} \cdot \boldsymbol{\lambda}$    ▷ Compute denominator sum
            $\boldsymbol{\lambda}_{increment} \mathrel{+}= \mathbf{t_i}/d$
        end for
        $\boldsymbol{\lambda}^{l+1} = \left(\boldsymbol{\lambda}^{l+1} \cdot \boldsymbol{\lambda}_{increment}\right)/\mathbf{s}$
    end for
return $\boldsymbol{\lambda}$
end procedure
```

5.3.2 System modelling

Due to the large dimensionality of the projection operators and large ammounts of data, system matrix cannot be formed and system modelling factors are computed in the runtime of the MLEM algorithm. They reflects the probability that event i originated in voxel j. The proposed system model is inspired by a model of [13] and presents a tradeoff between fidelity and computation complexity. There are three functions involved in the proposed model:

$$t_{ij} = R(\mathbf{e}, \mathbf{n}) \cdot K(\theta_{computed}, E_0) \cdot I(\theta_{diff}) \tag{5.5}$$

The first function R represents the probability that the photon reaches the detector in the first place. It is an approximation of the solid angle of the detector, that would be expensive to compute. The approximation considers the probability to be directly proportional to the normalized dot product of detector's normal $\mathbf{n}$ and emission vector $\mathbf{e}$ and inversely proportional to the square of distance from the voxel center. Futhermore, we assume that the probability of detecting a photon coming from behind the scatterer's plane is 0.

$$R(\mathbf{e}, \mathbf{n}) = \frac{\max(\frac{\mathbf{n} \cdot \mathbf{e}}{\|\mathbf{n}\|\|\mathbf{e}\|}, 0)}{\|\mathbf{e}\|^2}. \tag{5.6}$$

The second function K accounts for the probability, that the photon will undergo Compton scattering with an angle $\theta_{computed}$. It is given by the Klein-Nishina formula

$$\begin{aligned}
\theta_{computed} &= \arccos(\frac{\mathbf{n} \cdot \mathbf{e}}{\|\mathbf{n}\|\|\mathbf{e}\|}) \\
P(\theta_{computed}, E_0) &= \frac{1}{1 + \left(\frac{E_0}{m_e c^2}\right)[1 - \cos(\theta_{computed})]} \\
K(\theta_{computed}, E_0) &= \frac{1}{2}\alpha^2 r_c^2 P(\theta_{computed}, E_0)^2 \\
&\quad \left[P(\theta_{computed}, E_0) + P(\theta_{computed}, E_0)^{-1} - \sin(\theta_{computed})^2\right]
\end{aligned} \tag{5.7}$$

The last function reflects the uncertainty in the measurement and Doppler broadening and denotes a probability that a scattering angle θ_{real} will be measured as $\theta_{measured}$. It is modelled by the Normal distribution

$$\begin{aligned}
\theta_{diff} &= \|\theta_{real} - \theta_{measured}\| \\
I(\theta_{diff}) &= \frac{1}{\sqrt{2\pi\sigma^2}} e^{-\frac{(x-\mu)^2}{2\sigma^2}}
\end{aligned} \tag{5.8}$$

where σ is a tunable parameter.

5.3.3 Sensitivity calculation

Sensitivity is the general probability of detecting a photon that was emitted from voxel j given a list of sensing locations. It is apparent, that a voxel that is far away or behind the detector system has almost zero probability of being sensed even if it contains an emitting source.

Two sensitivity models were used in this thesis

- **Analytical model**
  The main idea of the sensitivity model is to approximate the space of all possible detections using point-wise evaluation of every detector's pixel (256x256). Given voxel j, we consider coordinates of every pixel in the every detector's sensing location and for each, compute the point-wise sensitivity function. The sensitivity value for voxel j is then sum of

point-wise sensitivities.

For the point-wise sensitivity function a model considering only the approximation of solid angle has been chosen (Equation 5.6). The low computational demand allows fast evaluation of the whole sensitivity model.

The full procedure is described in Algorithm 4.

Algorithm 4 Sensitivity computation - analytical method

```
procedure ComputeSensitivity(centers of voxels C, detector poses D)
    $\mathbf{s} = 0$                                  ▷ Initialize sensitivity vector
    for each voxel index $j$ do
        set $s[j] = 0$
        for each detector_pose index $k$ do
            for each detector_pixel $l$ do
                compute emission vector $\mathbf{e}$ and detector normal $\mathbf{n}$
                set $s[j] += R(\mathbf{e}, \mathbf{n})$      ▷ compute the point-wise sensitivity
            end for
        end for
    end for
  return $s$
end procedure
```

Monte Carlo method

The idea of the second proposed sensitivity model is to utilize the developed simulator and determine the sensitivity value experimentally. That is, we simulate a large number of photons emitted by a voxel j ($\approx 10^7 - 10^8$), follow their paths and count portion of the photons that resulted in a detected Compton events in one of the sensing locations. The steps are described in Algorithm 5.

Algorithm 5 Sensitivity computation - Monte Carlo method

```
procedure SimulateSensitivity(centers of voxels C, detector poses D,
  number of simulated photons per each voxel n)
    $\mathbf{s} = 0$                                  ▷ Initialize sensitivity vector
    for each voxel index $j$ do
        simulate $n$ photons emitting from voxel $j$
        $m$ = number of Compton events generated
        $s[j] = m/n$
    end for
  return s
end procedure
```

5.4 Regularization

Several techniques are proposed for the regularization of the reconstructed volumes.

5.4.1 MAP-EM

An extension of the LM-MLEM was proposed for regularization. After performing review of available methods, total variation (TV) was chosen as the prior because of its convenient denoising properties and low computation cost.

Two implementations of TV minimization were considered, namely the algorithm of Fadili/Peyré [45] was implemented in PyTorch and the algorithm of Chambolle [46] was used from the skimage Python library.

When implementing the MAP-EM with total variation prior, the idea is to compute a standard MLEM iteration as described in Algorithm 3, followed by an additional TV minimization smoothing step. The result of the TV minimization is then used in the next iteration of MLEM (see Algorithm 6).

Algorithm 6 MAP-EM

```
procedure ComputeMAP-EM(list of events I, centers of voxels C, detector poses D)
    Initialize lambda vector $\boldsymbol{\lambda}$ using backprojection
    Precompute sensitivity vector $\mathbf{s}$ given the detection geometries
    for each iteration $l$ do
        $\boldsymbol{\lambda}^{l+1/2}$ = ComputeLM-MLEMStep(I, C, D, $\boldsymbol{\lambda}^{l}$)
        $\boldsymbol{\lambda}^{l+1}$ = TV-Regularization($\boldsymbol{\lambda}^{l+1/2}$)
    end for
return $\boldsymbol{\lambda}$
end procedure
```

5.5 Summary

The whole project is depicted in Figure 5.1. Namely, simulator generates Compton data, that is preprocessed and passed into the reconstruction pipeline. There, backprojection is computed and then used as a prior for the MAPEM. Optionally, the result of MAPEM is also passed to the deep regularization network to obtain the final reconstruction.

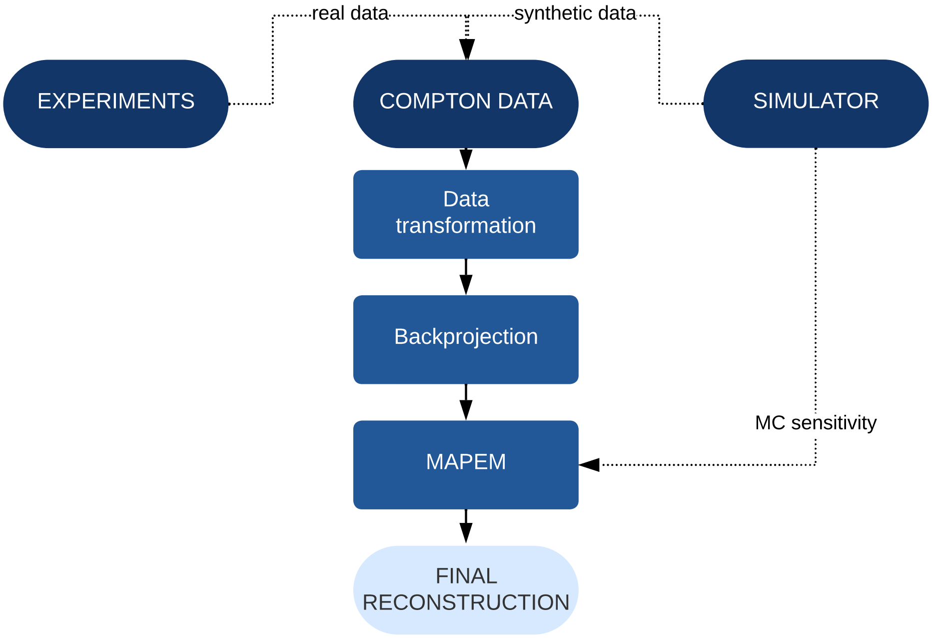

Figure 5.1: Schematics of the final solution flow.

5.6 Metrics

Various metrics are used to assess the reconstruction's quality and accuracy. These metrics help compare the reconstructed volume to the ground-truth volume and provide a quantitative measure. In this thesis, the metrics were computed after first scaling both prediction and ground-truth to interval [0, 1].

Mean square error (MSE)

MSE measure the mean of the squared differences between the reference and reconstructed image. MSE ranges from 0 to infinity, with 0 meaning a complete match.

$$\mathrm{MSE} = \frac{1}{N}\sum_{x,y,z}(\mathrm{Prediction}(x,y,z) - \mathrm{GT}(x,y,z))^2$$

Peak Signal-to-Noise Ratio (PSNR)

PSNR evaluates the quality of the reconstructed image relative to the reference image. It builds on the MSE, considering the maximum possible intensity value L. PSNR is usually expressed in logarithmical scale:

$$\mathrm{PSNR} = 10 \cdot \log_{10}\left(\frac{L^2}{\mathrm{MSE}}\right) \tag{5.9}$$

A higher PSNR value indicates a better match. In the case of a perfect match, MSE is 0, resulting in an undefined PSNR value. PSNR is most meaningful when comparing different reconstructed images to the same reference image.

SSIM

SSIM [56] is a widely metrics used for accessing structural similarity [57]. It takes into account the luminance, contrast and structural information to assess the similarity between the reference and reconstructed images. The SSIM values range from -1 to 1, with 1 indicating a perfect match.

$$\mathrm{SSIM}(A, B) = \frac{(2 \cdot \mu_A \cdot \mu_B + C_1)(2 \cdot \sigma_{AB} + C_2)}{(\mu_A^2 + \mu_B^2 + C_1)(\sigma_A^2 + \sigma_B^2 + C_2)} \tag{5.10}$$

A and B are the two 3D signals being compared, μ_A and μ_B are their respective mean values, σ_A and σ_B are their respective standard deviations, σ_{AB} is the covariance between A and B, and C_1 and C_2 are small constants to stabilize the division when the denominator is close to zero.

For computation, a window size is used to set the size of the local region. The default size of the window is 11, however, its choice depends on the specific application and scale of structures in the image. The function is evaluated on all possible positions and the output is combined to return the final SSIM value. This thesis adopts the window sizes of 3, 5 and 11 as they showed to express the most information in the context of the Compton data.

Chapter 6

Experiments and results

6.1 Conic projection methods

Figure 6.1 shows the difference between the proposed conic projection methods. Notice the widening of the cone in case of angular difference method and the sharp edges in step error function and faded edges in Normal error function.

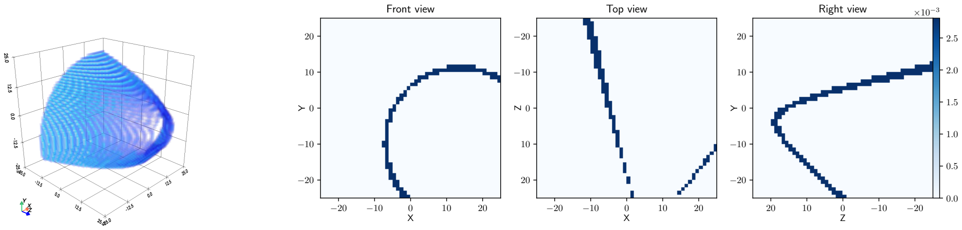

(a) : Angular difference distance function with binary step function error ($\tau = 3°$).

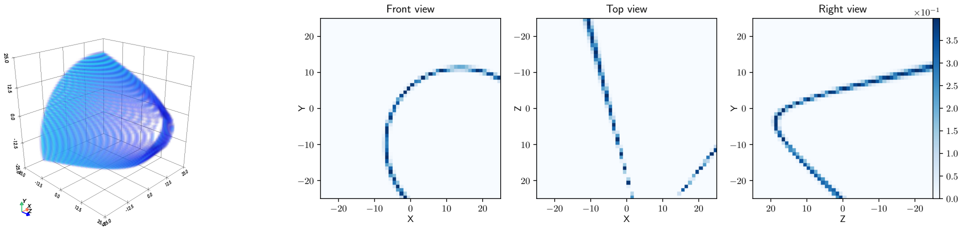

(b) : Perpendicular distance function with Normal error ($\sigma = 1°$)

Figure 6.1: Comparison of conic projection methods demonstrated using back-projection of one event.

Experimental evaluation showed that the best performance is achieved with either a combination of angular difference distance function and binary step function or with perpendicular distance function with Normal error function. The angular difference distance function better accommodates for the scattering angle uncertainty, however, it projects widening cones that present reconstruction problems in scenarios with large voxel grid (100x100x100). The perpendicular distance function generally performs well in most scenarios, however it exhibits limitations in situations with large scattering angle uncertainty.

6.1.1 Sensitivity

The results of the proposed sensitivity computation approaches are presented in Figures 6.2 6.3. The methods are evaluated on a grid of size 50x50x50. In case of 1 pose, a visible difference can be seen in the top view. Monte Carlo result shows the sensitivity to be more restricted in the direction of the incoming photon and less restricted to the distance. This difference is even more apparent in the case of 6 pose scenario.

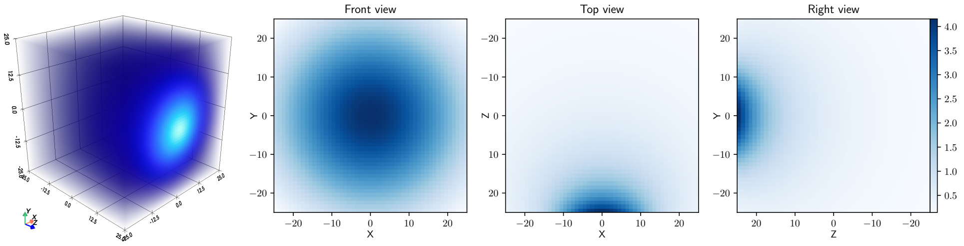

(a) : 1 pose - analytical sensitivity, integral approximated using 256x256 pixel centers, computation took 10.16s

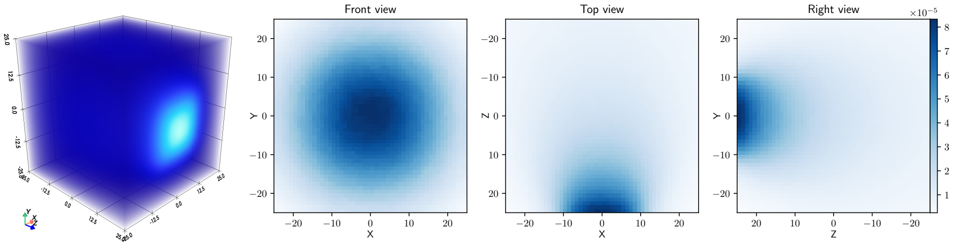

(b) : 1 pose - MC sensitivity, simulated 340 000 photons from each of the 125 000 sources, recorded 99 877 493 events, simulation ran for 1h 25min, results smoothed using median filter with kernel 3x3x3.

Figure 6.2: Comparison of sensitivity calculation methods - part 1.

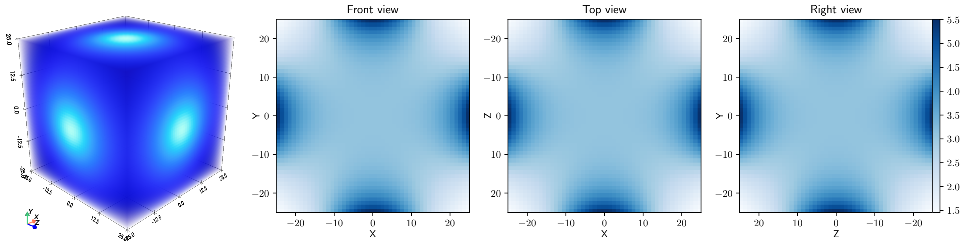

(a) : 6 poses - analytical sensitivity, integral approximated using 256x256 pixel centers, computation took 50.22s

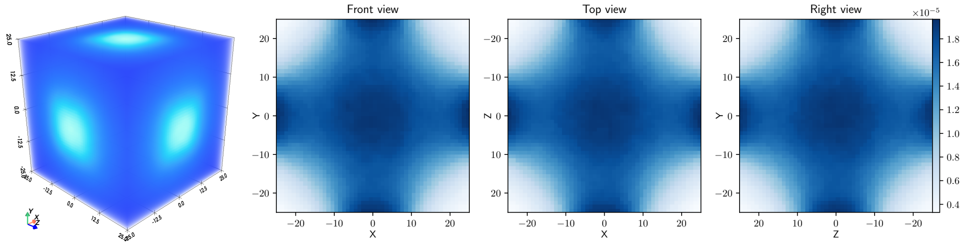

(b) : 6 poses - MC sensitivity, simulated 390 000 photons from each of the 125 000 sources, recorded 99 630 510 events, simulation ran for 1h 39min, results smoothed using median filter with kernel 3x3x3.

Figure 6.3: Comparison of sensitivity calculation methods - part 2.

Experiment was performed to asses the influence of the two sensitivity methods on the reconstruction outcome. A cylindrical phantom was simulated using the CoCam Sim from 6 poses ($5 \cdot 10^5$ events in total) and reconstructed using first the analytical sensitivity model and then the Monte Carlo sensitivity model. Figure 6.4 shows the results. Differences can be seen near the edges of the volume, as these are the areas outside of furthest away from the sensing locations.

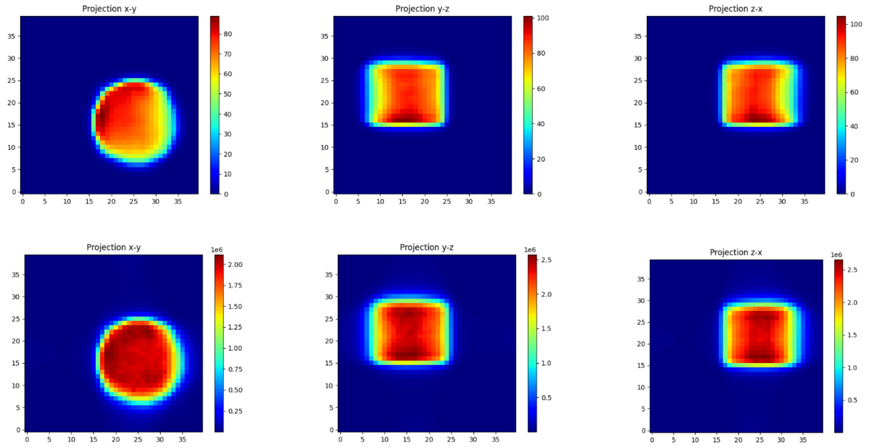

Figure 6.4: Demonstration of the effect of sensitivity function selection on the MLEM reconstruction outcome. First row presents reconstruction obtained using analytical sensitivity model, second row shows reconstruction obtained using Monte Carlo sensitivity

6.1.2 Total variation minimization

The total variation minimization methods were tested standalone on noised phantoms. Representative results on a sphere are outlined in Figure 6.5. The Fadili-Peyre's implementation often did not converge to the desired reference volume. Chambolle's algorithm performed better, and the only challenge was in the selection of regularization weight λ (not to mistake with the λ used in the Compton reconstruction context). In light of the above-mentioned, Chambolle's algorithm was selected for integration into the MAPEM algorithm.

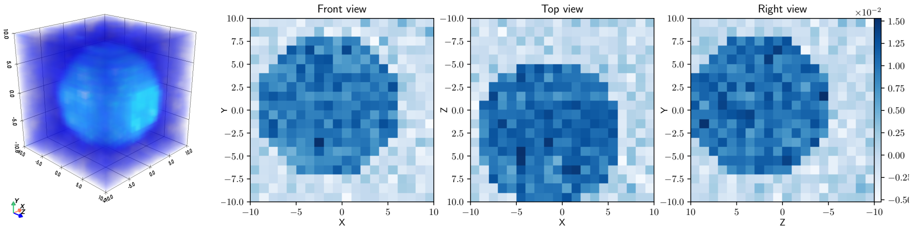

(a) : Input to the total variation minimization algorithms (3D view and slices) - the object is a simulated noised sphere phantom (not an actual output of the reconstruction).

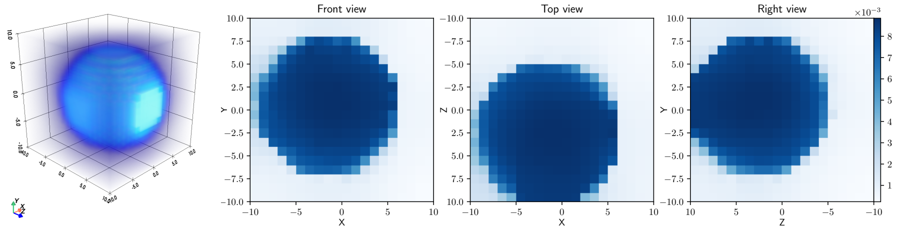

(b) : Result (3D view and slices) obtained using Chambolle's algorithm, with parameter $\lambda = 2$. Computation took 0.010s.

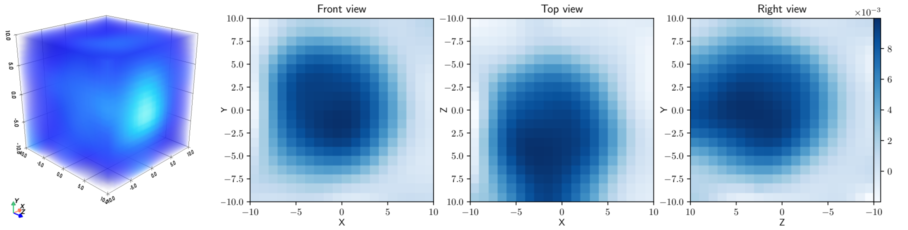

(c) : Result obtained using Fadili-Peyre's algorithm, with parameter $\kappa = 100$. Computation took 0.0027s.

Figure 6.5: Comparison of total variation minimization methods.

6.2 Demonstration of the complete method

6.2.1 Results on simulated data

An ellipsoidal phantom was used to demonstrate the quality of the reconstruction during different stages of the reconstruction pipeline. The results are presented in Figure 6.6.

Convergence of the MAPEM (and subsequently also MLEM) method is presented in Figure 6.7. The time requirements are described in Table 6.1.

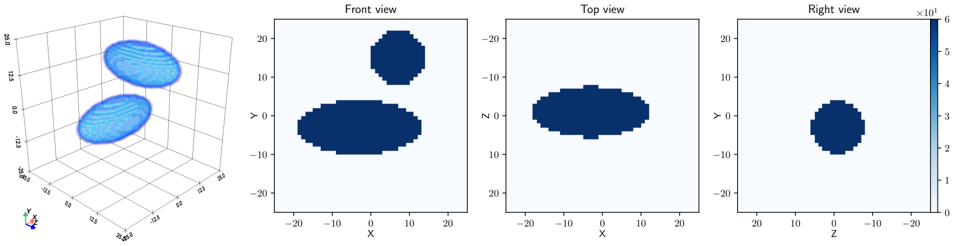

(a) : Ground truth source distribution.

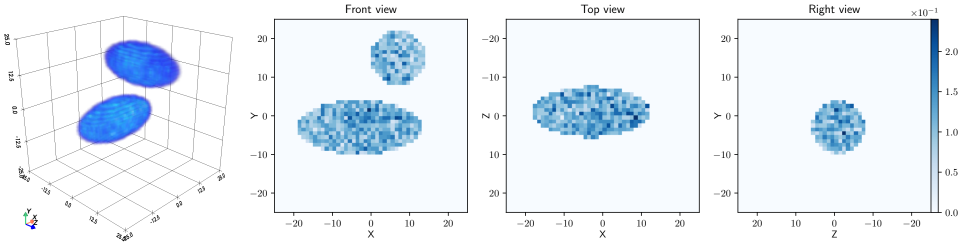

(b) : Ground truth source distribution according to the events detected. MSE 1.719e+07, SSIM3 9.384e-01, SSIM5 9.220e-01, SSIM11 8.964e-01.

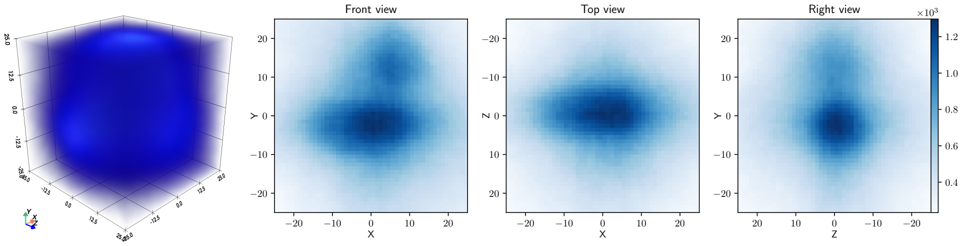

(c) : Result after backprojection, MSE 2.134e+09, SSIM3 2.300e-02, SSIM5 2.247e-02, SSIM11 2.612e-02.

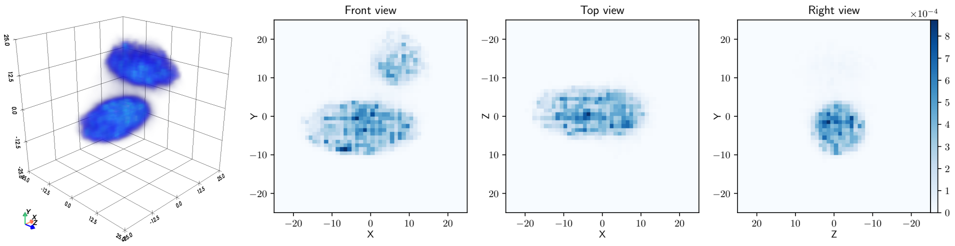

(d) : Results after 20 iterations of MLEM. MSE 1.721e+07, SSIM3 9.059e-01, SSIM5 8.838e-01, SSIM11 8.430e-01.

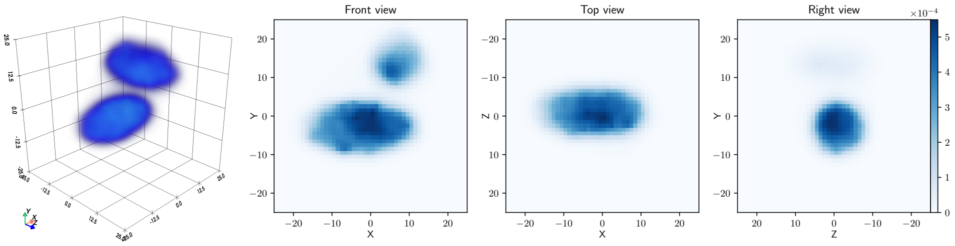

(e) : Results after 20 iterations of MAPEM (λ=33), MSE 1.721e+07, SSIM3 8.730e-01, SSIM5 8.739e-01, SSIM11 8.712e-01.

Figure 6.6: Comparison of different reconstruction methods on ellipsoidal phantom.

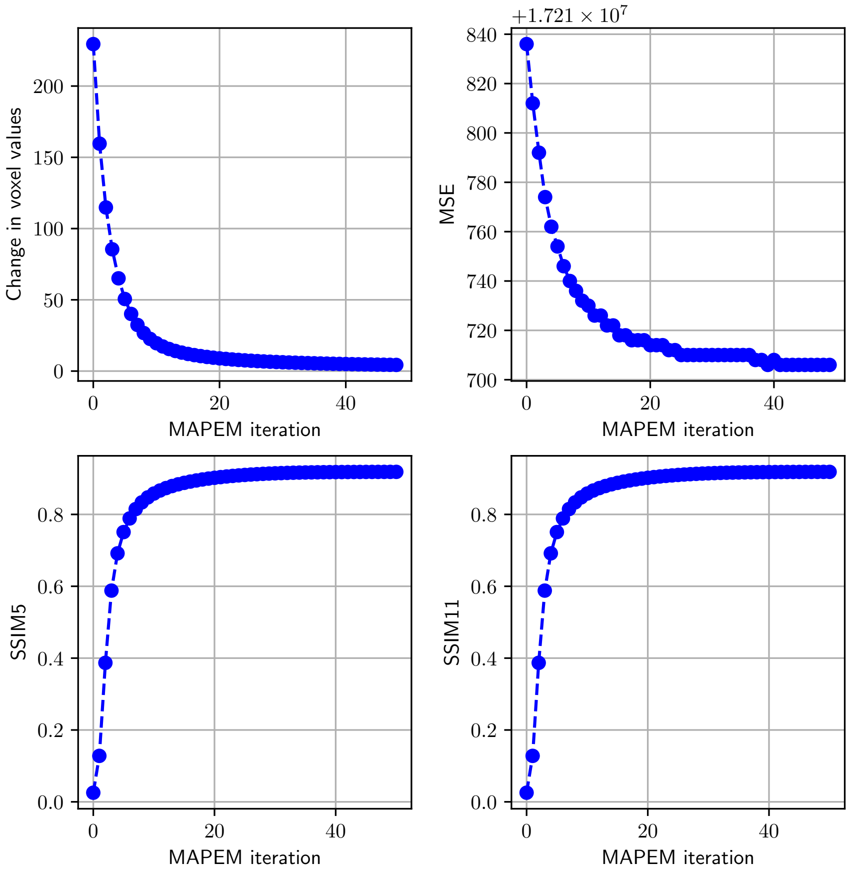

Figure 6.7: Convergence of MAPEM.

Method	Time duration
Preprocessing	5.22s
Backprojection	27.02s
One iteration	46.36s
DL inference	0.56s
Total time (20 iterations)	959.0s = 16minutes
Total time (50 iterations)	2349.8s = 39minutes

Table 6.1: Time requirements of the proposed method

6.2.2 Results on real data

The reconstruction method was validated using real measurements.

Concentric cylinder phantom

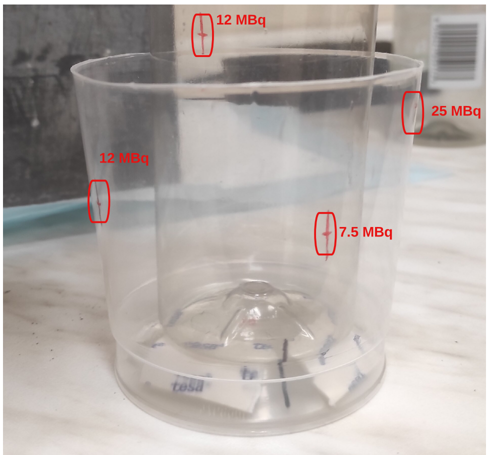

(a) : Front view of the experiment sample with marked locations and activities of the capsules (are not present in this image).

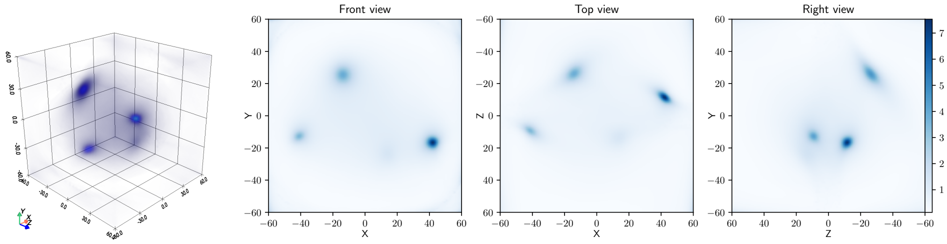

(b) : Results of the MAPEM reconstruction.

Figure 6.8: Reconstruction (3D view and projections) of the concentric cylinder phantom.

Figure 6.8 shows the results of the reconstruction. All of the capsules can be clearly identified and their location corresponds well. The activities of the capsules cannot be directly deduced from the intensities of the reconstructed image, however a relationship is present. The capsule with the least amount of activity (7.5 MBq) is barely visible, nevertheless it can be discerned.

Anthropomorphic human phantom

Figure 6.9 shows the results of the reconstruction for the case of measurement of whole human phantom as well as for only the insert. All of three capsules can be clearly identified and their location corresponds well, especially in case of the measurement of standalone insert. The quality of the reconstruction of the human phantom is decreased, due to the lower number of events and presence of scattering medium between the radioactive source and the detector. Elongation can be present in both of the reconstructions due to the limited viewing angle. The capsule with the highest activity can be recognized in both of the reconstructions.

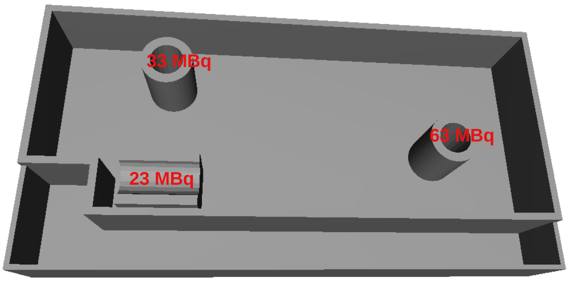

(a) : Top view of the experiment sample with marked locations and activities of the capsules

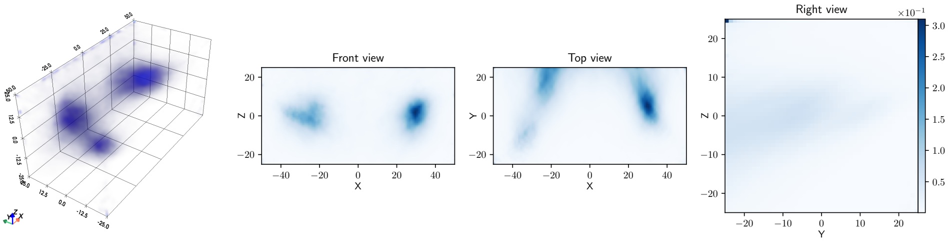

(b) : Reconstruction (3D view and projections) of the anthropomorphic human phantom, 40 406 Compton events were provided.

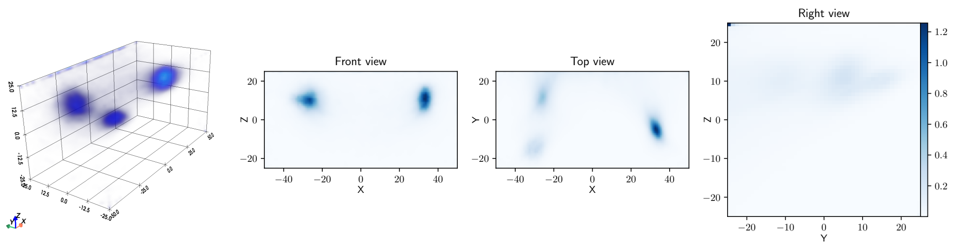

(c) : Reconstruction (3D view and projections) of the insert of the anthropomorphic human phantom, 81 505 Compton events were provided.

Figure 6.9: Reconstruction of the anthropomorphic human phantom. The position of the capsules was not the same in both scenarios, because the insert needed to be extracted from the phantom. See Figure 3.4 for description of the data.

6.2.3 Influence of number of events

To demonstrate the performance of the proposed method with different event numbers, a cross-shaped phantom was selected. This experiment evaluates the reconstruction pipeline for 1 046 058 events, 46 714 events and for 4 688 events.

The results are presented in Figure 6.10. In case of 1 046 058 events, nearly perfect reconstruction can be seen. In case of 46 714 events, the performance of the reconstruction method is still acceptable. However, with 4688 events, the reconstruction performs poorly and only a rough shape of the cross can be recognized.

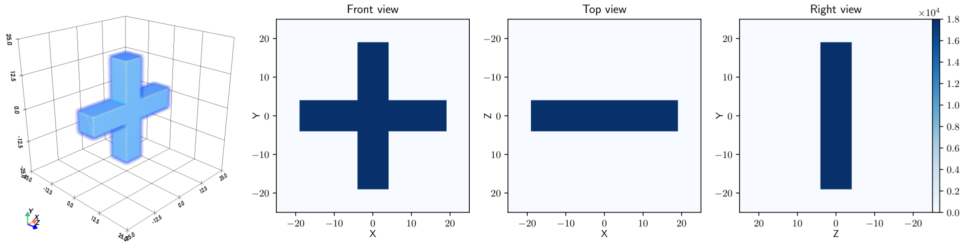

(a) : Ground-truth source distribution

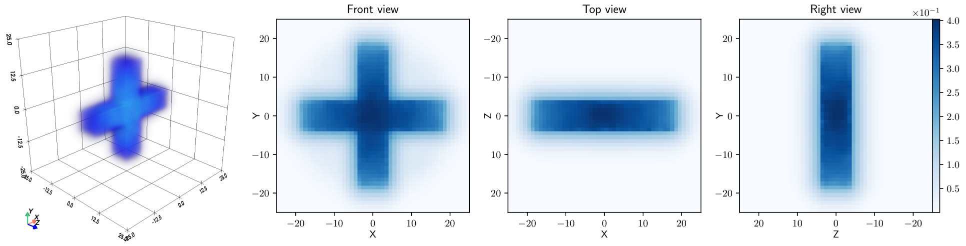

(b) : Results (3D view and slices) obtained with 1 046 058 events. MSE 6.345e+08, SSIM3 9.200e-01, SSIM5 9.251e-01, SSIM11 9.268e-01.

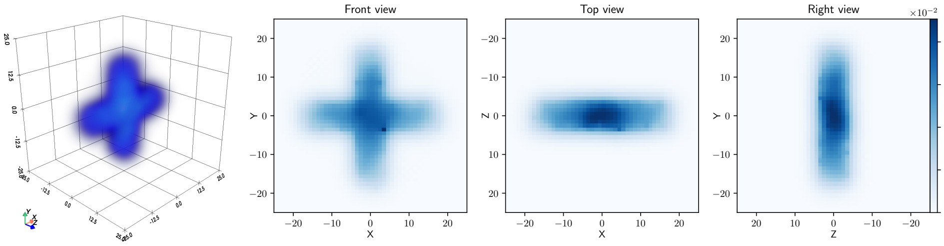

(c) : Results (3D view and slices) obtained with 46 714 events. MSE 1.253e+06, SSIM3 8.631e-01, SSIM5 8.622e-01, SSIM11 8.604e-01.

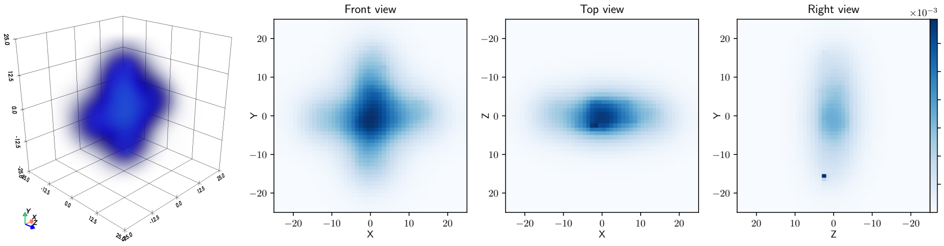

(d) : Results (3D view and slices) obtained with 4688 events. MSE 1.253e+04, SSIM3 7.830e-01, SSIM5 7.772e-01, SSIM11 7.710e-01.

Figure 6.10: Demonstration of reconstruction performance under different number of events. Cross phantom was generated using the CoCam Sim.

6.2.4 Influence of sensing locations

Another experiment was done to evaluate the performance of the reconstruction pipeline in case of limited sensing locations. A cylindrical phantom was selected and simulated. First scenario presents ideal situation where sensing is possible from each of the 6 sides of the voxel grid. Second case presents scenario, that is usual in case of thyroid measurement - only the frontal pose, along with four tilts of 50° (up, down, left, right) is possible. The last scenario considers measurement from one sensing location only.

Figure 6.11 shows that the proposed method works as expected in case of ideal number of sensing locations. Furthermore, even in a realistic scenario of thyroid measurement, the reconstruction is only slightly compromised. However, in case of only one sensing location available, the method suffers from lack of information.

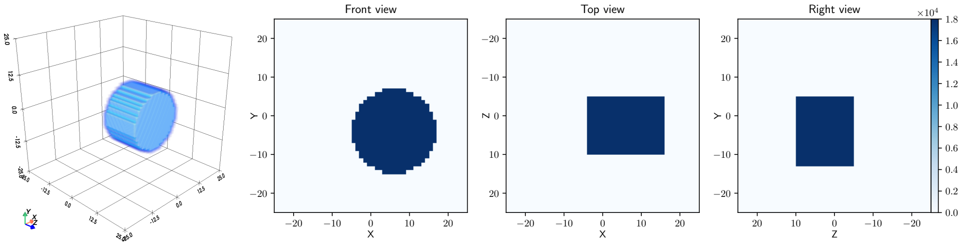

(a) : Ground truth source distribution.

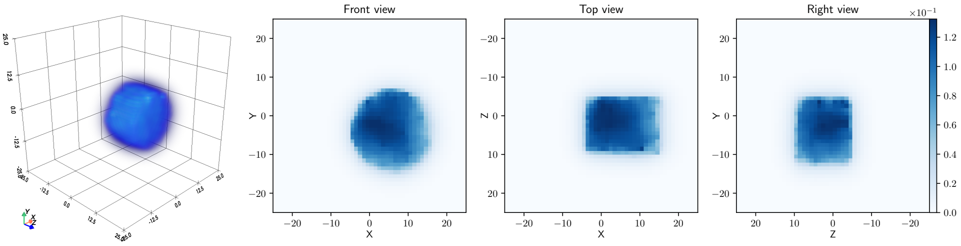

(b) : Results (3D view and slices) with 100k events, sensing from 6 poses. MSE 1.462e+07, SSIM3 8.972e-01, SSIM5 8.955e-01, SSIM11 8.945e-01.

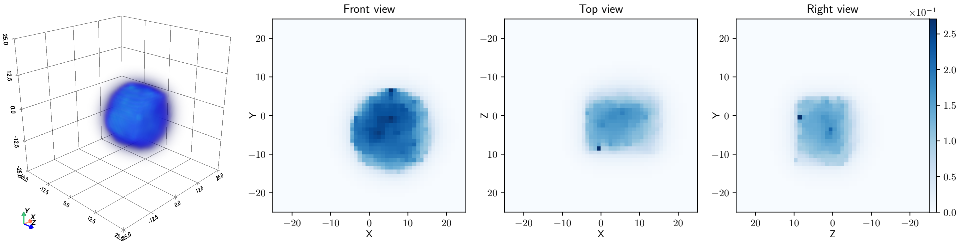

(c) : Results (3D view and slices) with 100k events, sensing from 5 poses (central projection and directional tilts of 50deg).MSE 1.462e+07, SSIM3 8.860e-01, SSIM5 8.845e-01, SSIM11 8.834e-01.

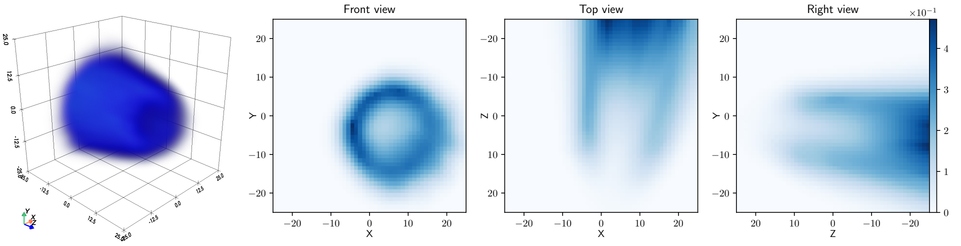

(d) : Results (3D view and slices) with 100k events, sensing from 1 pose. MSE 1.462e+07, SSIM3 7.755e-01, SSIM5 7.608e-01, SSIM11 7.327e-01.

Figure 6.11: Demonstration of reconstruction performance given different sensing locations. Cylinder phantom was simulated by the proposed simulator.

6.2.5 Influence of measurement errors

This experiment was motivated by the nature of uncertainty in the scattering angle measurement, that is present in the real world scenarios. A phantom comprising of three different-sized spheres was simulated using the CoCamSim (allows more detailed physics modelling). The scattering angles were generated with a Normally distributed noise with different values of σ. A control sample had an uncertainty of $\sigma = 0°$, followed by a sample with $\sigma = 3°$ that presents a typical uncertainty reported by the detector. The last two experiments were generated with $\sigma = 10°$. Both angular and perpendicular distance functions were evaluated.

Figure 6.12 shows the results of the experiments. The proposed method shows robust performance in case of $\sigma = 3°$. In case of $\sigma = 10°$, perpendicular distance function performs worse than the angular distance function. However, even with the angular distance function, the smallest sphere is more detected.

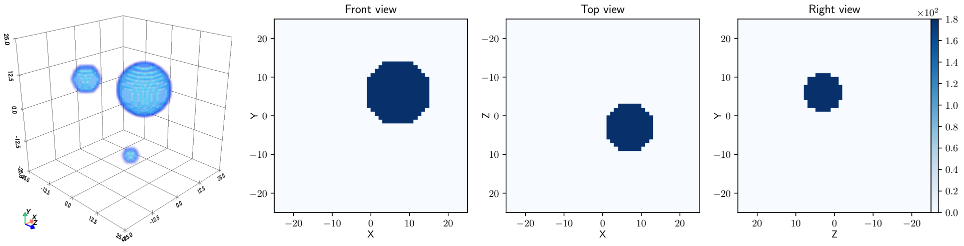

(a) : Ground truth source distribution.

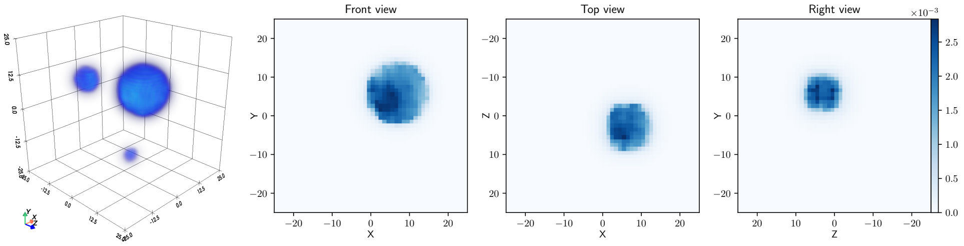

(b) : Results (3D view and slices) obtained with no scattering angle uncertainty 0° using perpendicular distance measure function. MSE 9.144e+06, SSIM3 9.388e-01, SSIM5 9.407e-01, SSIM11 9.355e-01.

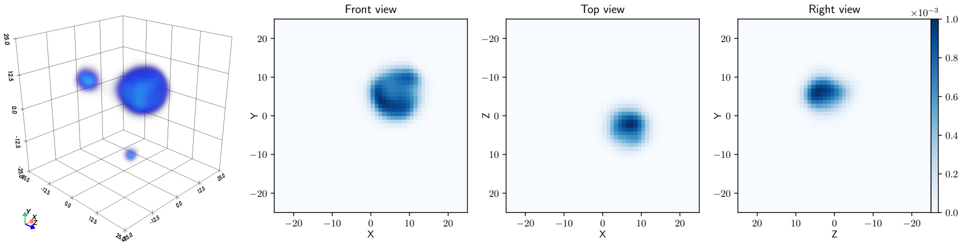

(c) : Results (3D view and slices) obtained with a scattering angle uncertainty of 5° using perpendicular distance measure function. MSE 9.144e+06, SSIM3 9.512e-01, SSIM5 9.381e-01, SSIM11 9.116e-01.

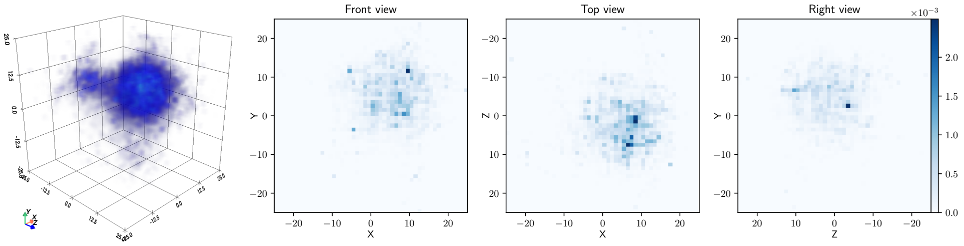

(d) : Results (3D view and slices) obtained with a scattering angle uncertainty of 10° using perpendicular distance measure function. MSE 9.145e+06, SSIM3 8.448e-01, SSIM5 8.307e-01, SSIM11 8.186e-01.

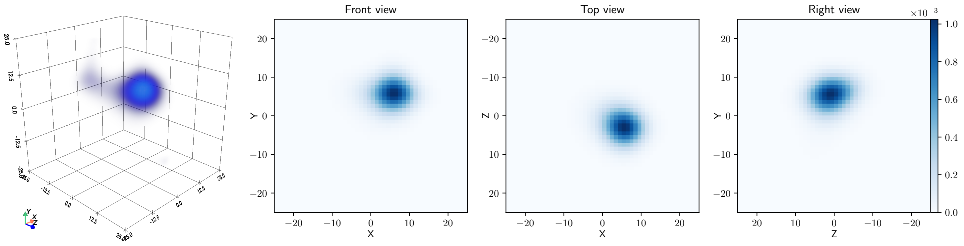

(e) : Results (3D view and slices) obtained with a scattering angle uncertainty of 5° using angular distance measure function. MSE 9.144e+06, SSIM3 9.421e-01, SSIM5 9.231e-01, SSIM11 8.879e-01.

Figure 6.12: Demonstration of reconstruction performance with scattering angle uncertainty using a spherical phantom generated by the CoCam Sim (100k events).

6.2.6 Influence of false events

Last experiment aimed to test the robustness of the reconstruction pipeline by incorporating false Compton events. This phenomenon occurs very often in the real data, especially in the case of high photon flux. In these situations, correct scatterer/absorber interaction pairing is challenging and incorrect correspondences are generated, leading to false Compton cones. This experiment aims to test the reconstruction at 0% of false events, 20% and 50%, using a conical phantom.

The Figure 6.13 presents decent performance in case of both 0% and 20% false events. With 50% of false events, the reconstruction quality is severely degraded and only a rough shape of the cone can be recognized.

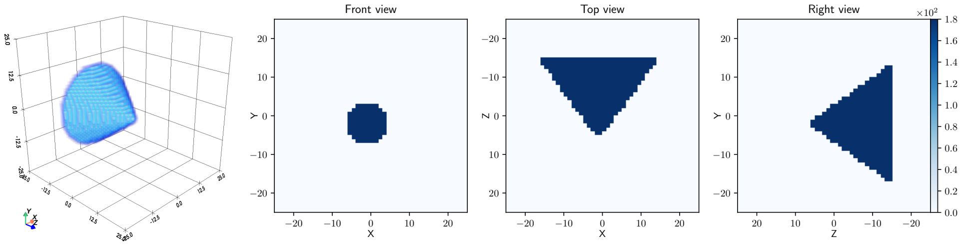

(a) : Ground truth source distribution.

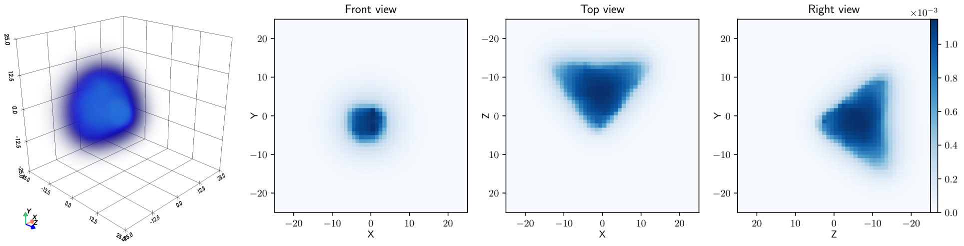

(b) : Results (3D view and slices) obtained with 0% false events present. MSE 1.475e+07, SSIM3 7.731e-01, SSIM5 7.762e-01, SSIM11 7.816e-01.

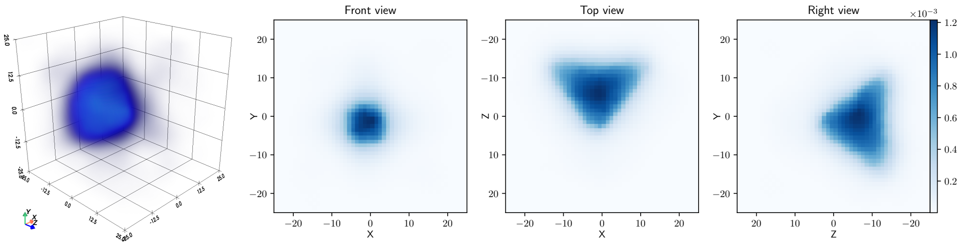

(c) : Results (3D view and slices) obtained with 20% false events present. MSE 1.475e+07, SSIM3 7.024e-01, SSIM5 7.054e-01, SSIM11 7.103e-01.

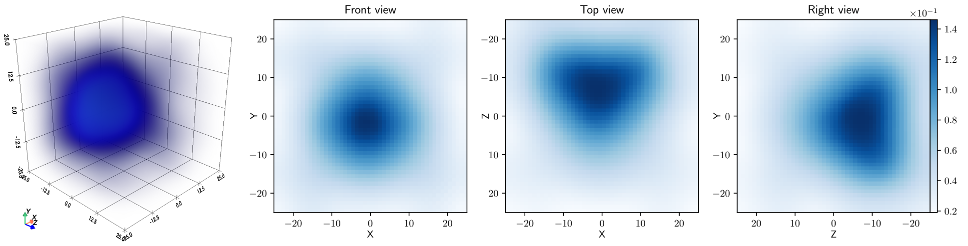

(d) : Results (3D view and slices) obtained with 50% false events present. MSE 1.475e+07, SSIM3 2.901e-01, SSIM5 2.957e-01, SSIM11 3.019e-01.

Figure 6.13: Demonstration of reconstruction performance with false coincidences presented on a conical phantom generated by the proposed simulator using 100k events.

Chapter 7

Discussion and conclusion

7.1 Discussion

Simulator

Let us first analyze the proposed data simulator. The biggest advantage of the simulator can be considered its computational speed and straightforward implementation. Even though the simulator includes only a simple physics model and does not account for more advanced phenomena such as the detection probability or Doppler broadening, it provided a vital tool for the validation of the reconstruction methods. The transition from the proposed simulator to a more sophisticated CoCam Sim did not introduce any unexpected phenomena in the reconstruction. This can be accounted to the fact that the impact of neglected phenomena is small.

MLEM

The presented results show that the selected reconstruction method is suitable for the application of 3D Compton reconstruction of radiopharmaceutical distribution. The experiments showed that the proposed analytical sensitivity was not ideal for the use with the Thyropix detector (Figure 6.4). The reason can be accounted to the missing geometrical properties (mutual arrangement of the detectors), as the model only considered distance and angle to the front detector. On the other hand, the Monte Carlo sensitivity provided an unexpected performance boost, probably caused by the ability to correctly model the abovementioned geometrical arrangement of the detectors. However, a high number (10^8) of events recorded was necessary to obtain a good sensitivity estimate, which considerably extended the time needed. Therefore the sensitivity approaches present a tradeoff between accuracy and time requirements. Thirdly, in cases of lower event count or non-ideal data, MLEM has often converged to a non-smooth solution (Figure 6.6). In such cases, it is assumed that the Poisson nature of the underlying principles introduced noise that was amplified in the MLEM algorithm, as reported by [13]. This motivated the implementation of regularization strategies.

Total variation regularization

The choice of total variation regularization is well described in the literature. However, the minimization problem is challenging. Chambolle's projection algorithm worked well (Figure 6.5). The weakness of the Chambolle's approach is the need for accurate tuning of the parameter λ. The presented results were obtained after experimenting with the parameters extensively. A similar parameter setting could be used for the same voxel grid and similar source, easing the difficulty. However, in clinical practice, this could not be relied on, and the process of finding the proper regularization weights would have to be automated.

MAPEM

The MAPEM reconstruction method with total variation prior provided more significant improvements of the MLEM than was anticipated. Especially, the MAPEM method provides robust performance even in lower numbers of events and limited sensing locations. The resolution of the reconstruction depends on the error in the measurement data. The following conclusions were drawn regarding the limitations of the proposed method: The minimum recommended number of events is in the order of $10^3 - 10^4$ (Figure 6.10), depending on the complexity of the source distribution. A higher number of events is associated with a higher reconstruction quality, and numbers around $10^4 - 10^5$ provide enough information for a reasonable reconstruction. The voxel grid must be sensed from multiple locations to obtain the spatial information of the source. However, the method is capable of reconstructing objects with a limited range of projection angles, as presented in Figure 6.11. It must be noted that the limited range of sensing locations can cause elongation in the unseen axes. In the context of uncertainties, the proposed method is more robust than anticipated and reconstructs volumes given data that contain scattering angle error up to $\sigma = 5\circ$ (Figure 6.12). Approximately 20% of false coincidental events can be present in the data without influencing the outcome (Figure 6.13).

Comparison with related work

Qualitatively speaking, results are comparable to state-of-the-art work. The reconstructions of uniform plane source presented by [53] are qualitatively comparable to the reconstructions of geometrical primitives used in this thesis. The experimental cylindrical phantom reconstruction of [28] resembles the cylindrical phantom reconstruction in this thesis (Figure 6.11) while reportedly relying on significantly more events. In comparison with these applications, the advantage of this thesis lies in its versatility and computational speed.

The findings of this thesis also confirm those found by Feng et at., especially the number of events required (Figure 4.5).

Direct quantitative comparison with other state-of-the-art approaches was hindered by the lack of dataset benchmarks or detailed method description and is therefore replaced by the demonstrated experiments and limitation assessment discussed above.

7.2 Conclusion

The purpose of this master's thesis was to develop a 3D Compton reconstruction method for the application of radionuclide examination of the thyroid gland. After briefly familiarizing with existing nuclear imaging modalities and thyroid cancer, this method focused on Compton camera imaging.

Available datasets and simulators were reviewed, and a Monte Carlo simulator was developed. We contributed with a dataset consisting of numerous geometrical primitives, which enables the validation of the reconstruction methods. Two experiments were also conducted to acquire real data.

This thesis investigated available reconstruction methods for the task of 3D reconstruction of near-field sources. Then, backprojection operators were proposed, and a baseline approach with an LM-MLEM algorithm was implemented. Results show that backprojections operators accurately track the conic surface. An analytical system model for MLEM was adopted. The sensitivity model was obtained both analytically and through a Monte Carlo simulation. The simulated model provided better performance. The reconstruction algorithm was accelerated, and the methods were optimized to work in the time-constrained environment.

To improve the quality of the reconstruction, a regularization approach was implemented. The regularization approach included LM-MAPEM with a total variation prior. Comparing MLEM and MAPEM approaches, MAPEM provided significantly better performance.

A final reconstruction algorithm was integrated into a pipeline and demonstrated. Several scenarios were presented, showing both strengths and limitations of the proposed method. The method provides similar qualitative performance as publicly available state-of-the-art methods while being versatile and time-sensitive. Experimental evaluation showed that this thesis provides a competitive approach which is practically useful and serves the needs required. The reconstruction method will be used in the ThyroPIX research project and potentially in the final clinical product, assisting both patients and clinicians in thyroid cancer imaging.

7.2.1 Future work

Further research could focus on the development of a method for automatical tuning of the λ parameter of the total variation method to automatize the reconstruction process.

It may also be worth further exploring the application of deep regularization (described in the Appendix B).

Last but not least, object detection and segmentation on the reconstructed volumes could be employed to assist in the diagnostic process of thyroid nodules.

Bibliography

[1] K. Patton and F. Bell, *Anthony's Textbook of Anatomy & Physiology - E-Book*. Elsevier Health Sciences, 2018. [Online]. Available: https://books.google.cz/books?id=_n1_DwAAQBAJ

[2] "Thyroid anatomy image." [Online]. Available: https://www.yourhormones.info/glands/thyroid-gland/ (Accessed 2023-05-06).

[3] S.-W. Lee, "SPECT/CT in the treatment of differentiated thyroid cancer," *Nuclear Medicine and Molecular Imaging*, vol. 51, no. 4, pp. 297–303, Feb. 2017. [Online]. Available: https://doi.org/10.1007/s13139-017-0473-x

[4] T. Carling and R. Udelsman, "Thyroid cancer," *Annual Review of Medicine*, vol. 65, no. 1, pp. 125–137, Jan. 2014. [Online]. Available: https://doi.org/10.1146/annurev-med-061512-105739

[5] "Thyroid pathologies." [Online]. Available: https://my.clevelandclinic.org/health/diseases/12210-thyroid-cancer (Accessed 2023-05-06).

[6] "Thyroid pathologies." [Online]. Available: https://generalsurgery.ucsf.edu/conditions--procedures/thyroid-cancer.aspx (Accessed 2023-05-06).

[7] M. Schlumberger and S. Leboulleux, "Current practice in patients with differentiated thyroid cancer," *Nature Reviews Endocrinology*, vol. 17, no. 3, pp. 176–188, Dec. 2020. [Online]. Available: https://doi.org/10.1038/s41574-020-00448-z

[8] A. Hackshaw, C. Harmer, U. Mallick, M. Haq, and J. A. Franklyn, "131i activity for remnant ablation in patients with differentiated thyroid cancer: a systematic review," *The Journal of Clinical Endocrinology & Metabolism*, vol. 92, no. 1, pp. 28–38, 2007.

[9] L. Navrátil and J. Rosina, *Medicínska biofyzika*. Grada, 2005. [Online]. Available: https://books.google.cz/books?id=IX7hAAAACAAJ

[10] "Types of radioactive decay." [Online]. Available: https://jackwestin.com/resources/mcat-content/atomic-nucleus/radioactive-decay-2 (Accessed 2023-05-06).

[11] X. Lojacono, "Image reconstruction for Compton camera with application to hadrontherapy," Theses, INSA de Lyon, Nov. 2013. [Online]. Available: https://theses.hal.science/tel-01081066

[12] R. K. Parajuli, M. Sakai, R. Parajuli, and M. Tashiro, "Development and Applications of Compton Camera: A Review," *Sensors*, vol. 22, no. 19, p. 7374, Sep. 2022. [Online]. Available: https://doi.org/10.3390/s22197374

[13] Y. Feng, "Modeling and regularization in tomographic reconstruction for Compton camera imaging," Theses, Université de Lyon, Oct. 2019. [Online]. Available: https://theses.hal.science/tel-02900652

[14] P. Tandon, D. Prakash, S. C. Kheruka, and N. N. Bhat, "Interaction of ionizing radiation with matter," in *Radiation Safety Guide for Nuclear Medicine Professionals.* Springer Nature Singapore, 2022, pp. 21–35. [Online]. Available: https://doi.org/10.1007/978-981-19-4518-2_3

[15] "Gamma camera principle." [Online]. Available: https://www.cyberphysics.co.uk/topics/radioact/GCamera.html (Accessed 2023-05-06).

[16] J. Kybic, "Medical Imaging Systems course at CTU FEE." [Online]. Available: https://cw.fel.cvut.cz/b202/courses/zsl/start (Accessed 2.5.2023).

[17] R. Powsner and E. Powsner, *Essential Nuclear Medicine Physics*, ser. Essentials. Wiley, 2008. [Online]. Available: https://books.google.cz/books?id=8jswRw_UMnsC

[18] T. Nakano, M. Sakai, K. Torikai, Y. Suzuki, S. Takeda, S. ei Noda, M. Yamaguchi, Y. Nagao, M. Kikuchi, H. Odaka, T. Kamiya, N. Kawachi, S. Watanabe, K. Arakawa, and T. Takahashi, "Imaging of ^{99m}Tc-DMSA and ^{18}F-FDG in humans using a Si/CdTe Compton camera," *Physics in Medicine & Biology*, vol. 65, no. 5, p. 05LT01, Feb. 2020. [Online]. Available: https://doi.org/10.1088/1361-6560/ab33d8

[19] "SPECT system." [Online]. Available: https://nchmd.org/health-library/articles/prc-20212630/ (Accessed 2023-05-06).

[20] "PET system." [Online]. Available: https://together.stjude.org/en-us/diagnosis-treatment/imaging-tests/pet-scans.html (Accessed 2023-05-06).

[21] S. Sergieva, M. Atanasova, and I. Terziev, "SPECT-CT modality for imaging of medullary thyroid cancer (MTC)," *Journal of Nuclear Medicine & Radiation Therapy*, vol. 08, no. 02, 2017. [Online]. Available: https://doi.org/10.4172/2155-9619.1000329

[22] “PET image.” [Online]. Available: http://www.aboutcancer.com/throat_anatomy_pet.htm (Accessed 2023-05-06).

[23] D. Turecek, J. Jakubek, E. Trojanova, and L. Sefc, “Compton camera based on Timepix3 technology,” *Journal of Instrumentation*, vol. 13, no. 11, pp. C11 022–C11 022, Nov. 2018. [Online]. Available: https://doi.org/10.1088/1748-0221/13/11/c11022

[24] A. H. Compton, “A quantum theory of the scattering of x-rays by light elements,” *Phys. Rev.*, vol. 21, pp. 483–502, May 1923. [Online]. Available: https://link.aps.org/doi/10.1103/PhysRev.21.483

[25] H. Tashima and T. Yamaya, “Compton imaging for medical applications,” *Radiological Physics and Technology*, vol. 15, no. 3, pp. 187–205, Jul. 2022. [Online]. Available: https://doi.org/10.1007/s12194-022-00666-2

[26] “Klein-Nishina distribution.” [Online]. Available: https://en.wikipedia.org/wiki/Klein%E2%80%93Nishina_formula (Accessed 2023-05-06).

[27] V. Schönfelder, A. Hirner, and K. Schneider, “A telescope for soft gamma ray astronomy,” *Nuclear Instruments and Methods*, vol. 107, no. 2, pp. 385–394, 1973.

[28] H. Tashima, E. Yoshida, H. Wakizaka, M. Takahashi, K. Nagatsu, A. B. Tsuji, K. Kamada, K. Parodi, and T. Yamaya, “3D compton image reconstruction method for whole gamma imaging,” *Physics in Medicine & Biology*, vol. 65, no. 22, p. 225038, Nov. 2020. [Online]. Available: https://doi.org/10.1088/1361-6560/abb92e

[29] A. Sweeney, “Compton imaging for homeland security,” 2014. [Online]. Available: https://livrepository.liverpool.ac.uk/id/eprint/17633

[30] R. Todd, J. Nightingale, and D. Everett, “A proposed γ camera,” *Nature*, vol. 251, no. 5471, pp. 132–134, 1974.

[31] “Geant4 Toolkit.” [Online]. Available: https://geant4.web.cern.ch/ (Accessed 2023-05-25).

[32] “GATE Software.” [Online]. Available: http://www.opengatecollaboration.org/ (Accessed 2023-05-25).

[33] “Uniform spherical sampling.” [Online]. Available: http://corysimon.github.io/articles/uniformdistn-on-sphere/ (Accessed 9.5.2023).

[34] Y. Feng, A. Etxebeste, D. Sarrut, J. M. Létang, and V. Maxim, “3D reconstruction benchmark of a Compton camera against a parallel hole gamma-camera on ideal data,” *IEEE Transactions on Radiation and Plasma Medical Sciences*, vol. 4, no. 4, pp. 479 – 488, 2020. [Online]. Available: https://hal.science/hal-02505759

[35] M. Frandes, B. Timar, and D. Lungeanu, “Image Reconstruction Techniques for Compton Scattering Based Imaging: An Overview,” *Current Medical Imaging Reviews*, vol. 12, no. 2, pp. 95–105, Mar. 2016. [Online]. Available: https://doi.org/10.2174/1573405612666160128233916

[36] M. Cree and P. Bones, “Towards direct reconstruction from a gamma camera based on Compton scattering,” *IEEE Transactions on Medical Imaging*, vol. 13, no. 2, pp. 398–407, Jun. 1994. [Online]. Available: https://doi.org/10.1109/42.293932

[37] “Classical reconstruction approaches.” [Online]. Available: https://imaging.rigaku.com/blog/how-does-ct-reconstruction-work (Accessed 2023-05-06).

[38] C. HANSEN, “Digital image processing for clinicians, part III: SPECT reconstruction,” *Journal of Nuclear Cardiology*, vol. 9, no. 5, pp. 542–549, Sep. 2002. [Online]. Available: https://doi.org/10.1067/mnc.2002.122899

[39] R. Basko, G. Zeng, and G. Gullberg, “Application of spherical harmonics to image reconstruction for the Compton camera,” *Physics in medicine and biology*, vol. 43, pp. 887–94, 04 1998.

[40] V. Maxim, M. Frandes, and R. Prost, “Analytical inversion of the Compton transform using the full set of available projections,” *Inverse Problems*, vol. 25, p. 095001, 08 2009.

[41] K. Lange and R. Carson, “EM reconstruction algorithms for emission and transmission tomography,” *Journal of computer assisted tomography*, vol. 8, pp. 306–316, 05 1984.

[42] R. Levkovilz, D. Falikman, M. Zibulevsky, A. Ben-Tal, and A. Nemirovski, “The design and implementation of COSEN, an iterative algorithm for fully 3-D listmode data,” *IEEE Transactions on Medical Imaging*, vol. 20, no. 7, pp. 633–642, Jul. 2001. [Online]. Available: https://doi.org/10.1109/42.932747

[43] A. Kak and M. Slaney, *Principles of Computerized Tomographic Imaging*, ser. Classics in Applied Mathematics. Society for Industrial and Applied Mathematics, 2001. [Online]. Available: https://books.google.cz/books?id=Z6RpVjb9_lwC

[44] L. I. Rudin, S. Osher, and E. Fatemi, “Nonlinear total variation based noise removal algorithms,” *Physica D: Nonlinear Phenomena*, vol. 60, no. 1-4, pp. 259–268, Nov. 1992. [Online]. Available: https://doi.org/10.1016/0167-2789(92)90242-f

[45] J. Fadili and G. Peyré, “Total variation projection with first order schemes,” *IEEE Transactions on Image Processing*, vol. 20, 03 2011.

[46] A. Chambolle, "An algorithm for total variation minimization and applications: Special issue on mathematics and image analysis," *Journal of Mathematical Imaging and Vision*, vol. 20, 01 2004.

[47] V. Panin, G. Zeng, and G. Gullberg, "Total variation regulated EM algorithm [SPECT reconstruction]," *IEEE Transactions on Nuclear Science*, vol. 46, no. 6, pp. 2202–2210, Dec. 1999. [Online]. Available: https://doi.org/10.1109/23.819305

[48] A. Sawatzky, C. Brune, F. Wubbeling, T. Kosters, K. Schafers, and M. Burger, "Accurate EM-TV algorithm in PET with low SNR," in *2008 IEEE Nuclear Science Symposium Conference Record*. IEEE, Oct. 2008. [Online]. Available: https://doi.org/10.1109/nssmic.2008.4774392

[49] M. Sakai, R. K. Parajuli, Y. Kubota, N. Kubo, M. Kikuchi, K. Arakawa, and T. Nakano, "Improved iterative reconstruction method for Compton imaging using median filter," *PLOS ONE*, vol. 15, no. 3, p. e0229366, Mar. 2020. [Online]. Available: https://doi.org/10.1371/journal.pone.0229366

[50] Z. Yao, Y. Xiao, B. Wang, Y. Liu, Q. Hou, L. Lu, and Z. Chen, "Study of 3D fast Compton camera image reconstruction method by algebraic spatial sampling," *Nuclear Instruments and Methods in Physics Research Section A: Accelerators, Spectrometers, Detectors and Associated Equipment*, vol. 954, p. 161345, Feb. 2020. [Online]. Available: https://doi.org/10.1016/j.nima.2018.10.023

[51] G. Daniel, O. Limousin, D. Maier, A. Meuris, and F. Carrel, "Compton imaging reconstruction methods: a comparative performance study of direct back-projection, SOE, a new Bayesian algorithm and a new Compton inversion method applied to real data with Caliste," *EPJ Web of Conferences*, vol. 225, p. 06006, 2020. [Online]. Available: https://doi.org/10.1051/epjconf/202022506006

[52] A. Andreyev, A. Sitek, and A. Celler, "Fast image reconstruction for Compton camera using stochastic origin ensemble approach," *Medical Physics*, vol. 38, no. 1, pp. 429–438, Dec. 2010. [Online]. Available: https://doi.org/10.1118/1.3528170

[53] A. Kishimoto, J. Kataoka, T. Taya, L. Tagawa, S. Mochizuki, S. Ohsuka, Y. Nagao, K. Kurita, M. Yamaguchi, N. Kawachi, K. Matsunaga, H. Ikeda, E. Shimosegawa, and J. Hatazawa, "First demonstration of multi-color 3D in vivo imaging using ultra-compact Compton camera," *Scientific Reports*, vol. 7, no. 1, May 2017. [Online]. Available: https://doi.org/10.1038/s41598-017-02377-w

[54] Y. Hatsukawa, T. Hayakawa, K. Tsukada, K. Hashimoto, T. Sato, M. Asai, A. Toyoshima, T. Tanimori, S. Sonoda, S. Kabuki, H. Kimura, A. Takada, T. Mizumoto, and S. Takaki, "Electron-tracking Compton camera imaging of technetium-95m," *PLOS*

ONE, vol. 13, no. 12, p. e0208909, Dec. 2018. [Online]. Available: https://doi.org/10.1371/journal.pone.0208909

[55] "RCI Info." [Online]. Available: http://rci.cvut.cz/ (Accessed 2023-05-25).

[56] Z. Wang, A. Bovik, H. Sheikh, and E. Simoncelli, "Image quality assessment: From error visibility to structural similarity," *IEEE Transactions on Image Processing*, vol. 13, no. 4, pp. 600–612, Apr. 2004. [Online]. Available: https://doi.org/10.1109/tip.2003.819861

[57] J. Nilsson and T. Akenine-Möller, "Understanding SSIM," 2020. [Online]. Available: https://arxiv.org/abs/2006.13846

[58] "PyTorch library." [Online]. Available: https://pytorch.org/ (Accessed 2023-05-25).

[59] O. Ronneberger, P. Fischer, and T. Brox, "U-Net: Convolutional Networks for Biomedical Image Segmentation," 2015. [Online]. Available: https://arxiv.org/abs/1505.04597

[60] N. Siddique, S. Paheding, C. P. Elkin, and V. Devabhaktuni, "U-net and its variants for medical image segmentation: A review of theory and applications," *IEEE Access*, vol. 9, pp. 82 031–82 057, 2021. [Online]. Available: https://doi.org/10.1109/access.2021.3086020

[61] S. S. Salehi, D. Erdogmus, and A. Gholipour, "Tversky loss function for image segmentation using 3D fully convolutional deep networks," 09 2017, pp. 379–387.

[62] C. D. Pain, G. F. Egan, and Z. Chen, "Deep learning-based image reconstruction and post-processing methods in positron emission tomography for low-dose imaging and resolution enhancement," *European Journal of Nuclear Medicine and Molecular Imaging*, vol. 49, no. 9, pp. 3098–3118, Mar. 2022. [Online]. Available: https://doi.org/10.1007/s00259-022-05746-4

[63] K. Gong, D. Wu, K. Kim, J. Yang, S. Tao, G. Fakhri, Y. Seo, and Q. Li, "MAPEM-Net: an unrolled neural network for Fully 3D PET image reconstruction," 05 2019, p. 102.

[64] A. Reader, G. Corda-D'Incan, A. Mehranian, C. da Costa-Luis, S. Ellis, and J. Schnabel, "Deep Learning for PET Image Reconstruction," *IEEE Transactions on Radiation and Plasma Medical Sciences*, vol. PP, pp. 1–1, 08 2020.

[65] A. Guazzo and M. Colarieti-Tosti, "Learned primal dual reconstruction for PET," *Journal of Imaging*, vol. 7, no. 12, p. 248, Nov. 2021. [Online]. Available: https://doi.org/10.3390/jimaging7120248

[66] A. S. Chaudhari, E. Mittra, G. A. Davidzon, P. Gulaka, H. Gandhi, A. Brown, T. Zhang, S. Srinivas, E. Gong, G. Zaharchuk, and H. Jadvar, "Low-count whole-body PET with deep learning in a multicenter and externally validated study," *npj Digital Medicine*, vol. 4, no. 1, Aug. 2021. [Online]. Available: https://doi.org/10.1038/s41746-021-00497-2

[67] "subtlePET website." [Online]. Available: https://subtlemedical.com/subtlepet/ (Accessed 2.5.2023).

[68] G. Daniel, Y. Gutierrez, and O. Limousin, "Application of a deep learning algorithm to Compton imaging of radioactive point sources with a single planar CdTe pixelated detector," *Nuclear Engineering and Technology*, vol. 54, no. 5, pp. 1747–1753, May 2022. [Online]. Available: https://doi.org/10.1016/j.net.2021.10.031

[69] S. Takashima, H. Odaka, H. Yoneda, Y. Ichinohe, A. Bamba, T. Aramaki, and Y. Inoue, "Event reconstruction of Compton telescopes using a multi-task neural network," *Nuclear Instruments and Methods in Physics Research Section A: Accelerators, Spectrometers, Detectors and Associated Equipment*, vol. 1038, p. 166897, Sep. 2022. [Online]. Available: https://doi.org/10.1016/j.nima.2022.166897

[70] N. Navarathna and M. Gobbert, "The Power of GPUs in Machine Learning to Improve Proton Beam Therapy for Cancer Treatment," 2022. [Online]. Available: https://mdsoar.org/handle/11603/26363

[71] O. Cicek, A. Abdulkadir, S. S. Lienkamp, T. Brox, and O. Ronneberger, "3D U-Net: Learning Dense Volumetric Segmentation from Sparse Annotation," 2016. [Online]. Available: https://arxiv.org/abs/1606.06650

[72] A. Wolny, L. Cerrone, A. Vijayan, R. Tofanelli, A. V. Barro, M. Louveaux, C. Wenzl, S. Strauss, D. Wilson-Sánchez, R. Lymbouridou, S. S. Steigleder, C. Pape, A. Bailoni, S. Duran-Nebreda, G. W. Bassel, J. U. Lohmann, M. Tsiantis, F. A. Hamprecht, K. Schneitz, A. Maizel, and A. Kreshuk, "Accurate and versatile 3D segmentation of plant tissues at cellular resolution," *eLife*, vol. 9, p. e57613, jul 2020. [Online]. Available: https://doi.org/10.7554/eLife.57613

Appendix A

Project structure

Due to the large scale of the project and various methods involved, the code repository was organized according to a modular structure, comprising the following components.

- `A_simulator`
- `B_dataset`
- `C_backprojection`
- `D_MLEM`
- `E_MAPEM`
- `F_deep_regularization`
- `G_utils`

The code was written with Python, utilizing mainly the PyTorch library [58]. Git repository was set up, and access is available on request.

A_simulator

Folder `A_simulator` contains codes for data generation. Subfolder `CoCamSim` contains the CoCamSim simulator, subfolder `VP_sim` contains the simulator proposed by this thesis. To set up the simulation, user has to first edit `simulation_config.yaml` and then run the `simulate.py` script.

B_dataset

Both input files and reconstructions are stored in the `B_dataset` folder. The structure is depicted in Figure A.1. For the input data folders, each

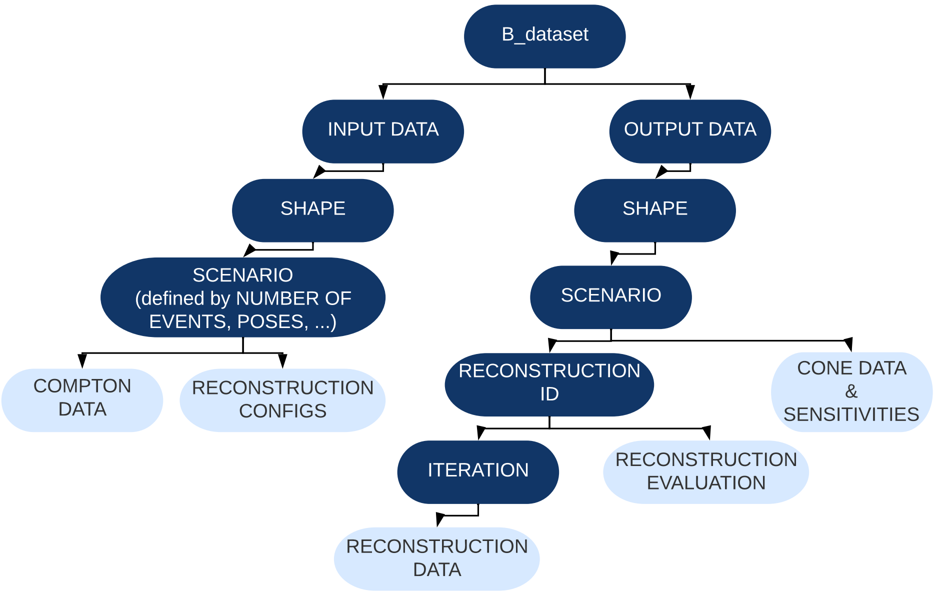

Figure A.1: Schematics of the dataset structure.

contains a subfolder with cone data in `txt` files named with the detector's pose. Along with that, there is a short textual description of the scenario and a prepared reconstruction configuration `yaml` file. The output data folders contain all products created in the reconstruction process - there is preprocessed Compton data file `cone_data_total.pt`, ground truth data folder, precomputed sensitivities file and the reconstructions themselves. They are organized in a hierarchical structure based on the voxel grid properties, reconstruction method and particular experiments. The experiment folder contains folders for each iteration data as well as final evaluation. In each iteration folder, there current model, metrics and 2D slices are provided.

C_backprojection

Folder `C_backprojection` provides routines for the conic projection and the code for running backprojection method. Furthermore, it also contains coordinate transformation procedure.

D_MLEM

The MLEM algorithm class is provided in folder `D_MLEM`. The folder contains implementations of system modelling and sensitivity computation approaches.

E_MAPEM

Folder `E_MAPEM` provides codes related to the MAPEM regularization approach. Namely, there are the implementations of the total variation along with experiment files that validate the approaches.

F_deep_regularization

`F_deep_regularization` folder contains the deep learning regularization pipeline. The Unet3D architecture implementation is stored in the `3dunet` folder. In addition to that, there is a subfolder `dl_data` that contain the dataset used, separated into training and validation parts. In `dl_utils` there is an aparatus for data import and output conversion, parameter grid search and evaluation of the method. Learned models and training logs are provided in the two remaining folders `dl_models` and `dl_logs`.

G_utils

This folder provides various codes and snippets for miscelaneous tasks needed in the project, such as visualisations, metric calculations, data conversion, bulk renaming, etc.

Appendix B

Deep regularization

B.1 Deep learning in Compton reconstruction

Motivation

The output of the image reconstruction process contains noise and inconsistencies. Deep learning could be deployed as an alternative to classical regularization approaches to improve the reconstructed images' quality by reducing noise and the presence of artefacts.

U-Net

U-Net [59] is a popular convolutional neural network architecture initially designed for biomedical image segmentation. It can be employed in both 2D and 3D images. U-Net has potential to be used for the task of deep regularization because of its simplicity and universality demonstrated by a wide range of existing applications [60].

U-Net has a characteristic U shape (Figure B.1), consisting of two parts – encoder and decoder, that are connected by intermediate and skip connections. The encoder presents a contracting path that consecutively shrinks the input image's dimensionality until a final feature tensor is reached. The decoder presents an expanding path that upsamples the feature tensor to reconstruct a final image. The skip connections allow for better preservation of spatial information.

There are many variants of U-Net depending on the used upsampling method, use of skip connections or dimensionality of the intermediate steps.

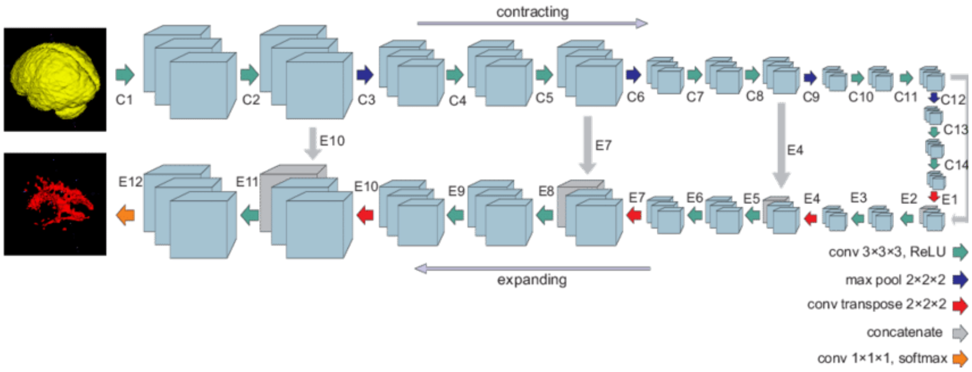

Figure B.1: Schema of the U-Net archtecture 3D implementation, source [61].

B.1.1 Existing deep learning applications

The usage of deep learning in nuclear imaging has emerged very recently, with the first applications in PET. Pain et al. [62] provided a review summarizing the usage of deep learning in PET.

Learnable components

In PET, deep learning is used in learnable components for existing iterative methods.

In MAPEM-Net [63], the convolutional neural network is combined with the MAPEM iterative algorithm. In each iteration, the current estimate is passed in parallel to U-Net (for denoising) and MAPEM and their outputs are fused.

A similar approach has been adopted in FSBEM-Net [64], which uses a parallel MAP-EM and CNN approach. Mehrain et al. trained the network with PET & MRI images to enhance the final output. Researchers used shallow networks, which reduced the necessary amount of training data to approx. 35 samples.

These methods work only with binned data available in PET/SPECT and can not be used with Compton data.

End-to-end neural network systems

Another type of approach implements end-to-end solutions using neural networks.

Learned primal-dual (LDP) method [65] combines two networks, where one network is taught to do the forward projection and the other to do the backprojection (in PET imaging). By chaining these networks into an iterative algorithm, reconstruction can be obtained. The method learns to encode the raw data into a cropped sinogram and decode it to reconstruct the reference image.

At present, these direct deep learning methods look to be impractical, having been demonstrated only for small 2-dimensional reconstructions. There is no availability to utilize physical understanding [62].

Postprocessing

The third application field employs deep learning in the postprocessing of the reconstruction. Several methods in PET have been used for enhancing resolution or decreasing acquisition time while maintaining the quality of the reconstruction.

The solution proposed by Chaudhari et al. [66] uses a 2.5D encoder–decoder U-Net to perform denoising on PET data.

Some commercial options, like FDA-approved subtlePET [67], are already available. SubtlePET has shown the ability to reduce the radiation dose to 25% while preserving PET image quality.

Applications in Compton imaging lag behind PET applications. Recent usage has been proposed by Daniel [68]. Their application was designed to improve the quality of 2D reconstruction images. First, researchers computed a backprojected image and used it as input for a CNN. The output of the CNN was a 2025 elements vector containing probabilities that the radioisotope source was in the direction given by discretized angles (longitudinal and latitudinal).

Event estimation and filtration

In the context of Compton imaging, deep learning has been used to estimate and filter event data.

Takashima et al. [69] worked with a single-layer Compton camera and used a neural network to determine the correspondences of photon interaction with the detector and estimate parameters of the Compton event.

Navarathna [70] used shallow networks for binary classification to filter out false events before image reconstruction. The approach was trained on 1,443,993 events and used 15 features.

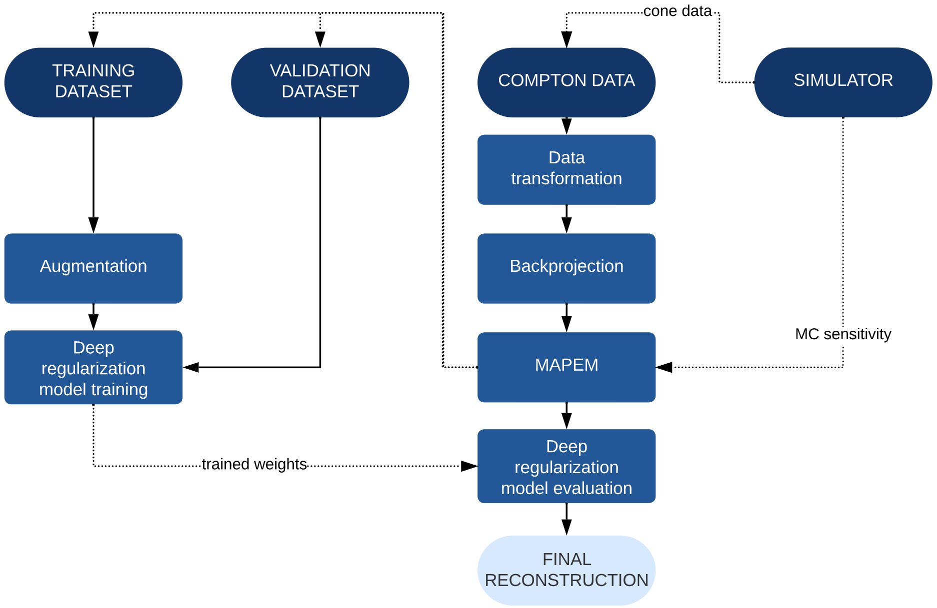

Figure B.2: Schematics of the proposed deep regularization solution flow.

B.1.2 Method description

A learning-based method is proposed to improve the outcome of the reconstruction method. Inspired by the PET denoising methods (Section B.1.1), the idea is that a simple CNN will learn to correct for the measurement uncertainties and incomplete model (see Figure B.2).

The proposed learning-based method uses a U-Net3D architecture [71], in particular its implementation by [72]. The architecture works with the voxel grid V of dimensions 50x50x50.

The models were trained on a specially created dataset consisting of 5 geometrical primitives (spheres, ellipsoids, crosses, cylinders and cones) in different spatial configurations (5 variants) and with different number of events (3 variants). The geometrical primitives were simulated, reconstructed using MAPEM and then used as input for the training. The labels were taken from the ground truth source distribution, provided by the simulator. The dataset was split into training and validation part (80/20 ratio). To enhance the training dataset, augmentations were used. Namely, training images were randomly flipped, rotated and shifted.

Several configuration of the U-Net feature layers (from 16 to 256), loss functions (L1, SmoothL1, L2) and input normalization (no normalization, [0, 1], [-1, 1]) were tested. Adam optimizer was selected.

The models were trained on the created dataset for 100 epochs. After each epoch, the model was evaluated on the validation dataset. The final model was selected after visually evaluating the performance on the validation dataset.

B.1.3 Selected results and discussion

Table B.1 shows the parameters of the network with the best outcome. The progress of the training is depicted in Figure B.3. Typical reconstruction is presented in Figure B.4.

Parameter	Value
Network	UNet3D
Features	16,32,64,128
Epochs	100
Optimizer	Adam
Learning rate	0.0002
Weight decay	0.00001
Loss	SmoothL1Loss

Table B.1: Parameters of the deep regularization network

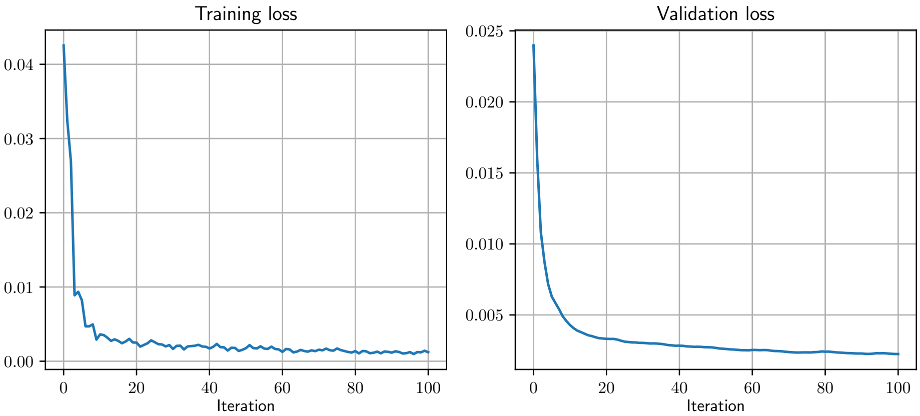

Figure B.3: Training progress of the deep regularization network.

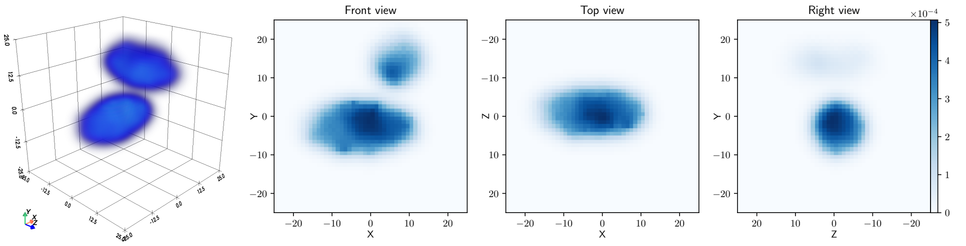

(a) : Output of the MAPEM reconstruction used as an input of the deep regularization.

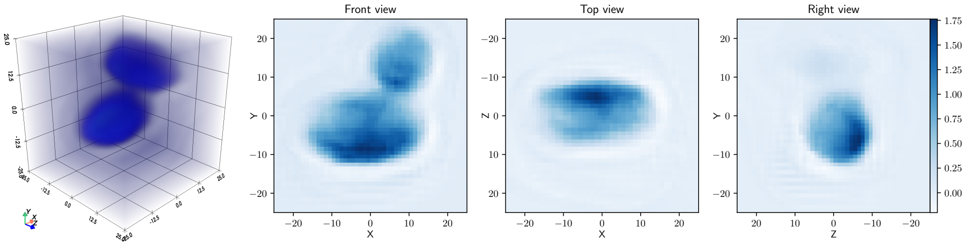

(b) : Output of the deep regularization.

Figure B.4: Sample evaluation of the deep regularization

Notice that the deep regularization lowered the ammount of noise near the ellipsoids, but at the cost of introducing significant ammount of noise in the whole volume. Compared to classical MAPEM implementation, deep regularization did not provide a significant advantage and was not therefore used in the reconstruction pipeline.

The proposed deep regularization method presented a simple solution to explore the potential use of learnable methods in Compton imaging. Fixed sized voxel grid was assumed, and a small-scale dataset was generated. The output of the network shows promising deblurring performance in some scenarios while introducing artefacts in others. Experimental work showed that the L1 and especially SmoothL1Loss were more appropriate than the L2 loss. Furthermore, the utilized augmentations showed a positive impact on the performance. We conclude that more positive results could be gained by

- utilizing loss functions more appropriate for 3D reconstruction, such as SSIM
- constructing and leveraging a large-scale dataset or taking advantage of transfer learning
- providing the network with additional information, such as sensitivity

This deep regularization is an open problem suggested for further work.